

1 **Projecting end of century climate extremes and their impacts on the**
2 **hydrology of a representative California watershed**

3
4 Fadjri Z. Maina^{1,3*}, Alan Rhoades², Erica R. Siirila-Woodburn¹, Peter-James Denny-Frank¹
5 ¹Energy Geosciences Division, Lawrence Berkeley National Laboratory 1 Cyclotron Road, M.S.
6 74R-316C, Berkeley, CA 94704, USA
7 ²Climate and Ecosystem Sciences Division, Lawrence Berkeley National Laboratory 1
8 Cyclotron Road, M.S. 74R-316C, Berkeley, CA 94704, USA
9 ³ now at NASA Goddard Space Flight Center, Hydrological Sciences Laboratory, Greenbelt,
10 MD, USA

11
12
13 *Corresponding Author: fadjizaouna.maina@nasa.gov

Deleted: the impacts of

Formatted: Centered, Indent: First line: 0", Space After: 14 pt, Line spacing: single

Formatted: Font: 16 pt, Bold, Font color: Black

Formatted: Font: 16 pt, Bold, Font color: Black

Formatted: Numbering: Continuous

Formatted: Font color: Custom Color(RGB(4,50,255))

Deleted: on the hydrology in California

Deleted: Projecting end of century climate extremes and hydrologic impacts on a representative California watershed

21 **Abstract**

22 In California, it is essential to understand the evolution of water resources in response to a
23 changing climate to sustain its economy and agriculture and to build resilient communities.
24 Although extreme conditions have characterized the historical hydroclimate of California, climate
25 change will likely intensify hydroclimatic extremes by the End of Century (EoC). However, few
26 studies have investigated the impacts of EoC extremes on watershed hydrology. We use cutting-
27 edge global climate and integrated hydrologic models to simulate EoC extremes and their effects
28 on the water-energy balance. We assess the impacts of projected driest, median, and wettest water
29 years under a Representative Concentration Pathway (RCP) 8.5 on the hydrodynamics of the
30 Cosumnes river basin. Substantial changes to annual average temperature, (>+2.5°C) and
31 precipitation (>+38%) will characterize the EoC extreme water years compared to their historical
32 counterparts. A shift in the dominant form of precipitation, mostly in the form of rain, is projected
33 to fall earlier. These changes reduce snowpack by more than 90%, increase peak surface water and
34 groundwater storages up to 75% and 23%, respectively, and drive the timing of peak storage to
35 occur earlier in the year. Because EoC temperatures and soil moisture are high, both potential and
36 actual evapotranspiration (*ET*) increase. The latter, along with the lack of snowmelt in the warm
37 EoC, cause surface water and groundwater stores to significantly decrease in summer, with
38 groundwater showing the highest rates of decrease. These changes result in more ephemeral EoC
39 streams with more focused flow and increased storage in the mainstem of the river network during
40 the summer.

41 **Keywords:** future climate extremes, integrated hydrologic model, global climate model, end of
42 century hydrology, watershed hydrology, water management

Deleted:

Deleted: High

Deleted:

Deleted: s

Deleted: Also,

Deleted: is

Deleted: s

Deleted: s

Deleted: makes

Deleted: these

Deleted: s

Deleted: Besides, the changes in the precipitation phase lead the lower-order streams to dry out in EoC summer whereas the mainstream experiences an increase in storage.

57 **Introduction**

58 California, the fifth largest economy in the world, hosts one of the largest agricultural
59 regions in the United States and is home to over 39 million people. Because of its geographic
60 location, Mediterranean climate, geology, and landscape, the state of California is sensitive to
61 climate change (Hayhoe et al. 2004). Understanding how water resources will evolve under a
62 changing climate is crucial for sustaining the state’s economy and agricultural productivity. The
63 region is especially susceptible to climate change given its reliance on the Sierra Nevada Mountain
64 snowpack as a source of water supply (e.g., Dettinger & Anderson, 2015). Studies show that
65 temperatures may warm by as much as 4.5°C by the End of Century (hereafter, EoC) (Cayan et
66 al., 2008), ~~that snowpack is expected to decrease as most precipitation will fall as rain instead of~~
67 snow (Siirila-Woodburn, et al., 2021), and ~~that~~ rain on snow events will exacerbate melt (Cayan
68 et al., 2008; Gleick, 1987; Maurer, 2007; Mote et al., 2005; Musselman, Clark, et al., 2017;
69 Musselman, Molotch, et al., 2017; Rhoades, Ullrich, & Zarzycki, 2018a). Given that precipitation
70 falls predominantly in winter months and the summers are hot and dry, the snow accumulated
71 during the winter provides important water storage for the dry season and is crucial to meet urban
72 demand, sustain ecosystem function, and maintain agricultural productivity (Bales et al., 2006;
73 Dierauer et al., 2018). As such, any significant reduction in the snowpack ~~has the potential to~~
74 ~~drastically affect the hydrology of the state~~ (Barnett et al., 2005; Harpold & Molotch, 2015; Milly
75 et al., 2005; Rhoades et al., 2018 a,b).

76 Over the past several decades, researchers have worked to understand how changes in
77 Sierra Nevada snowpack ~~will affect important hydrologic fluxes such as~~ evapotranspiration (Tague
78 & Peng, 2013) and streamflow (Berghuijs et al., 2014; Gleick, 1987; He et al., 2019; Maurer, 2007;
79 Safeeq et al., 2014; Son & Tague, 2019; Vicuna & Dracup, 2007; Vicuna et al., 2007). ~~For~~

Deleted: and

Deleted: will

Deleted: during both dry and wet periods,

Deleted: will affect

84 example, analyses of recent historical trends show that reductions in snowpack result in increases
85 in winter streamflow and decreases in the summer streamflow (e.g. Safeeq et al., 2012). However,
86 the sensitivity of a given area to these climatic changes depends on many factors including geology
87 and therefore drainage efficiency, topography, and land cover (Alo & Wang, 2008; Christensen et
88 al., 2008; Cristea et al., 2014; Ficklin et al., 2013; Mayer & Naman, 2011; Safeeq et al., 2015; Son
89 & Tague, 2019; Tang et al., 2019).

90 Climate change in California is also expected to lead to unprecedented extreme conditions,
91 which include both severe drought and intense deluge (Swain et al., 2018). In recent years, these
92 changes have already been observed in the forms of multi-year droughts (Cook et al., 2004; Griffin
93 & Anchukaitis, 2014; Shukla et al., 2015) and high-intensity precipitation events mainly caused
94 by atmospheric rivers (Dettinger et al., 2004; Dettinger, 2011; Dettinger, 2013; Ralph & Dettinger,
95 2011; Ralph et al., 2006). Periods without regular precipitation will require water management
96 strategies to adapt to ensure demands are met. Similarly, risk management plans and/or
97 infrastructure for floods, landslides, and other water surplus associated hazards (such as dam
98 failure) may also require reconsideration. This will be especially true if periods of precipitation,
99 including those associated with atmospheric rivers, become more extreme, variable, and occur
100 over a shorter window of time (Swain et al., 2018; Gershunov et al., 2019; Huang et al., 2020;
101 Rhoades et al., 2020b; Rhoades et al., 2021). Changes in water availability due to climate
102 “whiplash” will also have important ramifications for water resource management (Wang et al.,
103 2017; Swain et al., 2018) and significantly increase annual flood damages based on the level of
104 global warming that occurs (Rhoades et al., 2021). For example, in just the last two decades,
105 California has experienced the most severe drought in the last 1200 years (Griffin & Anchukaitis,
106 2014) followed by the wettest year on record (Di Liberto, 2017; SCRIPPS, 2017). These changes

Deleted: A

108 in meteorological patterns may become the “new normal”, raising several outstanding questions
109 related to how these changes in climate will impact the integrated hydrologic cycle, and
110 subsequently water resource availability for humans and ecosystems.

111 To project how changes in climate will impact watershed behavior, high-resolution,
112 physics-based models are one of the most promising ways to simulate system dynamics accurately,
113 particularly those that are non-linear, and constitute a better way to analyze a no-analog future than
114 the models used in the previous works. Previous studies analyzed future hydrologic conditions in
115 California but relied on models that do not 1) account for the interactions, feedbacks, and
116 movements of water from the lower atmosphere to the subsurface; 2) represent groundwater
117 dynamics and lateral flow; 3) incorporate physics-based high-resolution climate models and/or 4)
118 hydrologic models (e.g., Berghuijs et al., (2014); Gleick, (1987); He et al., (2019); Maurer, (2007);
119 Safeeq et al., (2014); Son & Tague, (2019); Vicuna & Dracup, (2007); Vicuna et al., (2007)).
120 Considerations of coupled interactions which explicitly account for groundwater connections are
121 important (Condon et al., 2020, 2013; Maxwell and Condon, 2016), especially given groundwater
122 is the largest reservoir in the terrestrial hydrologic budget and integral to water resource
123 availability. Also, previous studies have focused on the mid-century period (e.g. Maurer & Duffy,
124 2005; Son & Tague, 2019), which may indicate a more muted signal in hydrologic impacts than at
125 EoC. Understanding these impacts are essential because long-term climate projections show that
126 extremes will be more frequent and significant by the EoC (Cayan et al., 2008).

127 In this work, we assess the impacts of EoC extremely dry and intensely wet conditions on
128 the hydrodynamics of a Californian watershed that contains one of the last naturally flowing rivers
129 in the state. This allows us to investigate the impacts of climate change without the complexity of
130 active water management, and thus to set the context for water management decisions. We

131 specifically investigate how the water and energy balance respond to climate extremes under
132 climate change, and how those changes propagate to alter the spatiotemporal distribution of water
133 in different hydrologic compartments of the watershed. We focus our investigation on the changes
134 in groundwater and surface water storages. The balance of these two natural reservoirs, and their
135 relationship in response to changes in snowpack reservoir changes, is important for water
136 management decision making. We aim to 1) strengthen our physics-based understanding of the
137 main hydrologic processes controlling changes in water storages under a changing climate, 2)
138 quantify the magnitude and timing of these shifts in storage, and 3) identify the areas that are most
139 vulnerable to change.

Deleted: hydrologic

Deleted: climate

140 To do so, we utilize a novel combination of cutting-edge climate and hydrologic model
141 simulations. We use an integrated hydrologic model (ParFlow-CLM; Maxwell & Miller, 2005),
142 which solves the water-energy balance across the Earth's critical zone. When projecting
143 hydrologic flows, ParFlow-CLM's explicit inclusion of three-dimensional groundwater flow is
144 important given its demonstrated role in impacting land surface processes like evapotranspiration
145 (Maxwell & Condon, 2016). We drive Parflow-CLM with climate forcing from a physics-based,
146 variable-resolution enabled global climate model (the Variable Resolution enabled Community
147 Earth System Model, VR-CESM; Zarzycki et al., 2014) that dynamically couples multi-scale
148 interactions within the atmosphere-ocean-land system. This novel pairing of models allows for
149 several key considerations not present in other methods. Our approach represents both dynamical
150 and thermodynamic atmospheric response to climate change across scales, different from "pseudo-
151 global warming" and "statistical delta" approaches used in many hydrologic modeling studies
152 (e.g., Foster et al., 2020; Rasmussen et al., 2011). While these approaches are useful to isolate the
153 impact of a given perturbation and/or variable, expected changes in climate will involve the co-

156 evolution of many processes, and may therefore not account for compensating factors. The
157 interaction between dynamical and thermodynamic responses has important, and sometimes,
158 offsetting effects on features such as atmospheric rivers. For example, Payne et al. (2020) show
159 that the thermodynamic response to climate change enhances atmospheric river characteristics
160 (e.g., Clausius-Clapeyron relationship), whereas the dynamical response diminishes atmospheric
161 river characteristics (e.g., changes in the jet stream and storm track landfall location). Therefore,
162 VR-CESM may simulate a more inclusive hydroclimatic response to climate change in the western
163 United States at a resolution that is at the cutting-edge of today's global climate modeling
164 capabilities for decadal-to-centennial length simulations (Haarsma et al., 2016).

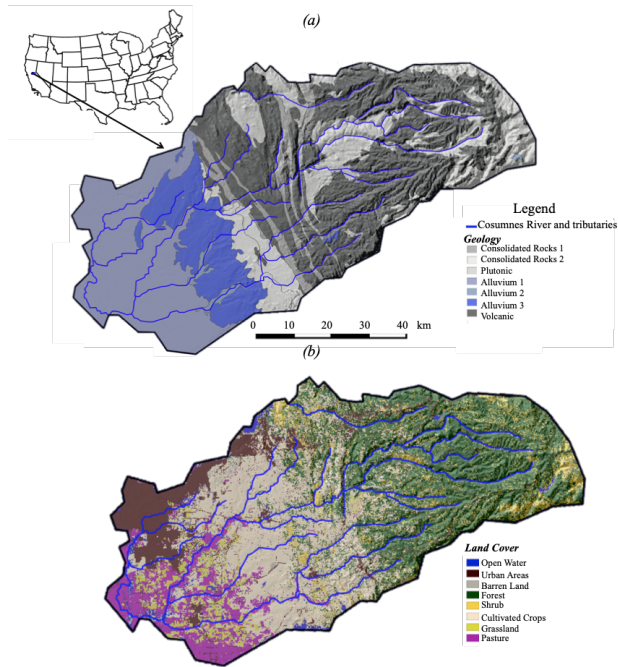
165 We perform these couplings on spatial and temporal scales relevant for atmosphere-to-
166 land, and land-to-subsurface interactions, an important consideration, given the recent work
167 showing the importance of meteorological forcing resolution in representing the hydrologic cycle
168 (Kampanhout et al., 2019; Maina et al., 2020b; Rhoades et al., 2016; Rhoades, Ullrich, Zarzycki,
169 et al., 2018c; Wu et al., 2017). Climate conditions for EoC (2070-2100) and a 30-year historical
170 period (1985-2015) are simulated to identify the median, wettest, and driest water year (WY) in
171 each. We then simulate the subsequent watershed hydrology of each year using ParFlow-CLM
172 forced with those meteorological conditions,

Deleted: e
Deleted: of each of the WYs

174 1. The Cosumnes watershed

175 The Cosumnes River is one of the last rivers in the western United States without a major
176 dam, offering a rare opportunity to isolate the impacts of a changing climate on the hydrodynamics
177 without reservoir management consideration (Maina et al., 2020a; Maina and Siirila-Woodburn,
178 2020). The watershed spans the Central Valley-Sierra Nevada interface and therefore represents

181 important aspects of the large-scale hydrology patterns of the state, namely the assessment of
182 interactions between changes in precipitation, snowpack, streamflow, and groundwater across
183 elevation and geologic gradients. Located in Northern California, USA, the Cosumnes watershed
184 is approximately 7,000 km² in size (Figure 1) and is between the American and the Mokelumne
185 Rivers. Its geology ranges from low-permeability rocks typical of the Sierra Nevada landscape
186 (volcanic and plutonic) to the porous and permeable alluvial depositions of the Central Valley
187 aquifers. These are separated by very low-permeability marine sediments. The watershed
188 topography includes a range of landscapes typical of the region (e.g. varying from flat agricultural
189 land, rolling foothills, and steep mountainous hillsides), and elevation varies from approximately
190 2500 m in the upper watershed to sea level in the Central Valley (Figure 1). The Sierra Nevada
191 mountains are characterized by evergreen forest while the Central Valley hosts an intensive
192 agricultural region including crops such as alfalfa, vineyards, as well as pastureland. Like other
193 Californian watersheds, the climate in the Cosumnes is Mediterranean consisting of wet and cold
194 winters (with a watershed average temperature equal to 0°C) and hot and dry summers (with
195 watershed average temperature reaching 25°C) (Cosgrove et al., 2003).



196

197 Figure 1: The Cosumnes Watershed (a) location and geology (Jennings et al., 1977), the alluvium
 198 in blue corresponds to the Central Valley aquifers whereas the consolidated rocks in gray
 199 correspond to the Sierra Nevada and cross-cutting marine sediments, and (b) land cover (Homer
 200 et al., 2015).

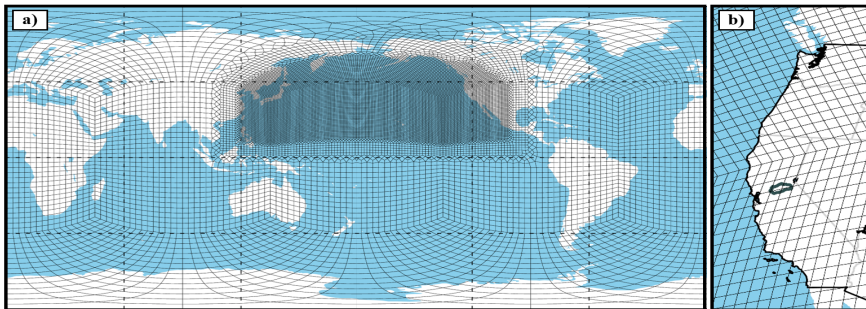
201

202 2. Experimental Design

203 2.1. Variable Resolution Community Earth System Model (VR-CESM)

204 Historical and EoC meteorological forcings are obtained from a simulation using the VR-
 205 CESM at a regionally refined resolution of 28 km over the Northern Pacific Ocean through the
 206 western United States, including the Cosumnes watershed and a global resolution of 111 km

207 (Figure 2). CESM has been jointly developed by NCAR (National Center for Atmospheric
208 Research) and the DOE (U.S. Department of Energy) and simulates a continuum of Earth system
209 processes including the atmosphere, land surface, land ice, ocean, ocean waves, and sea ice and
210 the interactions between them (Collins et al., 2006; Gent et al., 2011; Hurrell et al., 2013). VR-
211 CESM is a novel tool to perform dynamical downscaling as it allows for the interactions between
212 the major components of the global climate system (e.g., atmosphere, cryosphere, land surface,
213 and ocean) while allowing for regional-scale phenomena to emerge where regional refinement is
214 applied, all within a single model (Huang et al., 2016; Rhoades et al., 2016; Rhoades, Ullrich, &
215 Zarzycki, 2018b; Rhoades, Ullrich, Zarzycki, et al., 2018c).



216
217 Figure 2: Variable Resolution Community Earth System Model (VR CESM) grid for (a) globe and
218 (b) coastal western US with the Cosumnes watershed overlaid in dark gray.

219

220 The atmospheric model used for these simulations is the Community Atmosphere Model
221 (CAM) version 5.4 with the spectral element dynamical core, with an atmospheric dynamics time
222 step of 75 seconds, an atmospheric physics time step of 450 seconds, a prognostic treatment of
223 rainfall and snowfall in the microphysics scheme (Gettelman and Morrison, 2015) and run under
224 Atmosphere Model Intercomparison Project (AMIP) protocols (Gates, 1992). Under the AMIP
225 protocols, the atmosphere and land-surface components of the Earth system model are coupled

226 and periodically bounded by monthly observed sea-surface temperatures and sea-ice extents.
227 Although this configuration does not exactly recreate historical water years and events, it is
228 expected to reasonably simulate the distribution of water year types. Also, it should be noted that
229 the model only projects future conditions, within the envelope of plausible future conditions of the
230 RCP8.5 scenario and its assumptions of greenhouse gas emissions, sea-surface temperatures, and
231 sea ice extents and would not be expected to exactly forecast individual water years. Simulations
232 with VR-CESM are performed for 30-year periods based on the climates from a historical period
233 (1985-2015) and an EoC period (2070-2100). EoC simulations, analogous to Rhoades, Ullrich, &
234 Zarzycki, 2018, are bounded by estimates of future changes in ocean conditions derived from a
235 fully-coupled bias-corrected CESM simulation (assuming historical ocean simulation biases will
236 be similar in the future simulation) and forced by greenhouse gases and aerosol concentrations
237 assumed in the RCP8.5 emissions scenario. Historical VR-CESM outputs have been compared
238 with reanalyses and future VR-CESM outputs have been analyzed for shifts in
239 hydrometeorological extremes in further detail in Rhoades et al., 2020 a,b. To couple the outputs
240 with ParFlow-CLM, we regrid the unstructured 28km VR-CESM data over the Cosumnes
241 watershed using bilinear interpolation in the Earth System Modeling Framework (Jones, 1999) to
242 a final resolution of approximately 11 km (i.e. 57 grids over the Cosumnes watershed). Notably,
243 each of the spectral elements in the VR-CESM grid, shown in Figure 1, has a 4x4 set of Gauss–
244 Lobatto–Legendre (GLL) quadrature nodes where equations of the atmospheric model are solved
245 (Herrington et al., 2019). Therefore, the actual resolution at which the atmospheric dynamics and
246 physics are solved in VR-CESM are at higher-resolution (~28km) than is shown in Figure 1,
247 making these some of the highest resolution global Earth system model simulations over California
248 to date (Haarsma et al., 2016).

Deleted: The atmospheric model used for these simulations is the Community Atmosphere Model (CAM) version 5.4 with the spectral element dynamical core, with an atmospheric dynamics time step of 75 seconds, an atmospheric physics time step of 450 seconds, a prognostic treatment of rainfall and snowfall in the microphysics scheme (Gettelman and Morrison, 2015) and run under Atmosphere Model Intercomparison Project (AMIP) protocols (Gates, 1992). Under the AMIP protocols, the atmosphere and land-surface components of the Earth system model are coupled and periodically bounded by monthly observed sea-surface temperatures and sea-ice extents. include coupling the atmosphere-land-surface models and monthly-prescribed sea-surface temperatures and sea-ice extents. Although this configuration does not exactly recreate historical water years and events, it reasonably simulates the historical average conditions. Also, it should be noted that the model only projects future conditions which encapsulate the envelope of plausible future scenarios given greenhouse gas emissions, sea-surface temperatures, and sea ice extents and does not forecast individual future events..

Deleted: o

271 To identify if VR-CESM is fit for purpose to simulate historical dry, median, and wet WYs,
272 and inform potential biases in future projections (over California and, more specifically, the
273 Cosumnes watershed), we first conduct a model comparison to a widely used observational
274 product, the Parameter-elevation Relationships on Independent Slopes Model (PRISM; Daly et al.,
275 2008) at 4 km resolution analogous to Rhoades et al., (2020a). However, in this study, we focus
276 our assessment of VR-CESM fidelity over California and the Cosumnes watershed. PRISM
277 provides daily precipitation, mean dewpoint temperature and maximum and minimum surface
278 temperature, and vapor pressure. PRISM precipitation and temperature data spanning 1981-2019
279 are compared with the VR-CESM 1985-2015 simulations. We note that a mismatch in time period
280 (1981-2019 versus 1985-2015) is deliberate. VR-CESM is simulated under AMIP-protocols
281 (bounded by monthly observed sea-surface temperatures and sea-ice extents), and therefore we do
282 not expect VR-CESM to exactly recreate past historical WYs. However, we do expect that our
283 30-year simulation can reasonably recreate the range of WY types over California and the
284 Cosumnes, which is why we utilize the broader range of PRISM WYs that are available. For this
285 comparison, we regrid the unstructured VR-CESM data to 4km resolution (the native resolution
286 of PRISM) using the Earth System Modeling Framework (ESMF) Offline Re-gridding Weight
287 Generator in the NCAR Command Language (NCL, 2021).

288 The comparison (discussed in appendix A) indicates that VR-CESM reasonably reproduces
289 the historical WY conditions (i.e., interannual range of PRISM precipitation largely overlaps with
290 the range of model bias simulated by VR-CESM). VR-CESM generally simulates a wetter
291 historical period over the Cosumnes (range of bias of 1330 mm) relative to PRISM (range of
292 interannual variability of 1320 mm). Basin-average minimum (421 mm) and maximum (1740 mm)
293 WY accumulated precipitation are slightly larger than those of PRISM. Of relevance to this study,

294 PRISM has shown notable uncertainties in the Sierra Nevada. Lundquist et al., 2015 showed that
 295 an underrepresentation of the most extreme storm total precipitation in the Sierra Nevada can result
 296 in an upper-bound uncertainty of 20% in WY accumulated precipitation in PRISM. Therefore, the
 297 wettest WY simulated by VR-CESM is well within the 20% uncertainty range of PRISM's wettest
 298 WY (1580 ± 316 mm). Further, differences in basin-average WY accumulated precipitation
 299 between VR-CESM and PRISM are non-significant using a t-test and assuming a p-value < 0.05.
 300 As discussed in further detail below, we posit that atmospheric river-related precipitation is likely
 301 the driver of the wet bias mismatch with PRISM. However, we also note that the uncertainty
 302 bounds of the PRISM product WY precipitation totals in the Sierra Nevada are estimated to be
 303 upwards of ~20% too dry (e.g., Lundquist et al., 2015), particularly for extreme precipitation
 304 events such as atmospheric rivers and in mountainous terrain.

305

306 **2.2. Integrated Hydrologic Model: ParFlow-CLM**

307 The integrated hydrologic model ParFlow-CLM (Kollet & Maxwell, 2006; Maxwell, 2013;
 308 Maxwell & Miller, 2005) solves the transfer and interactions of water and energy from the
 309 subsurface to the lower atmosphere including: groundwater dynamics, streamflow, infiltration,
 310 recharge, evapotranspiration, and snow dynamics. The model describes 3D groundwater flow in
 311 variably saturated media with the Richards equation (equation 1, Richards, 1931) and 2D overland
 312 flow with the kinematic wave equation (equation 2).

$$313 \quad S_S S_W(\psi_P) \frac{\partial \psi_P}{\partial t} + \phi \frac{\partial S_W(\psi_P)}{\partial t} = \nabla \cdot [K(x) k_r(\psi_P) \nabla(\psi_P - z)] + q_s \quad (1)$$

314 Where is S_S the specific storage (L^{-1}), $S_W(\psi_P)$ is the degree of saturation (-) associated
 315 with the subsurface pressure head ψ_P (L), t is the time (T), ϕ is the porosity (-), k_r is the relative

316 permeability (-), z is the depth, q_s is the source/sink term (T^{-1}) and $K(x)$ is the saturated hydraulic
317 conductivity ($L T^{-1}$).

318 [ParFlow solves the mixed form of the Richards equation which has the advantage of](#)
319 [conserving the mass \(Celia et al., 1990\).](#)

320 The kinematic wave equation is used to describe surface flow in two dimensions is defined
321 as:

$$322 \quad -k(x)k_r(\psi_0)\nabla(\psi_0 - z) = \frac{\partial\|\psi_0,0\|}{\partial t} - \nabla \cdot \mathbf{v}\|\psi_0,0\| - q_r(x) \quad (2)$$

323 Where ψ_0 is the ponding depth, $\|\psi_0,0\|$ indicates the greater term between ψ_0 and 0, \mathbf{v} is
324 the depth averaged velocity vector of surface runoff ($L T^{-1}$), q_r is a source/sink term representing
325 rainfall and evaporative fluxes ($L T^{-1}$).

326 Surface water velocity at the surface in x and y directions, (v_x) and (v_y) respectively, is
327 computed using the following set of equations:

$$328 \quad v_x = \frac{\sqrt{S_{f,x}}}{m} \psi_0^{\frac{2}{3}} \text{ and } v_y = \frac{\sqrt{S_{f,y}}}{m} \psi_0^{\frac{2}{3}} \quad (3)$$

329 Where $S_{f,x}$ and $S_{f,y}$ friction slopes along x and y respectively and m is the manning coefficient.

330 ParFlow employs a cell-centered finite difference scheme along with an implicit backward Euler
331 scheme and the Newton Krylow linearization method to solve these nonlinear equations. The
332 computational grid follows the terrain to mimic the slope of the domain (Maxwell, 2013).

333 [ParFlow has many advantages in comparisons to other hydrologic models. Compared to](#)
334 [other hydrologic models \(MODFLOW \(Harbaugh, 2005\), FEFLOW \(Trefry and Muffels, 2007\),](#)
335 [SWAT \(Soil and Water Assessment Tool\) \(Neitsch et al., 2000\), SAC-MA \(Sacramento Soil](#)
336 [Moisture Accounting Model\)\), ParFlow has the advantages of accounting for land surface](#)
337 [processes such as snow dynamics and evapotranspiration and their interactions with the subsurface](#)
338 [which are crucial for studying the hydrology of California. ParFlow also solved the subsurface](#)

Formatted: Font color: Auto

Deleted: →→→

Formatted: Indent: First line: 0.5"

340 flow by accounting for variably saturated conditions, an important feature for calculating
341 groundwater recharge and the connection between the groundwater and the land surface processes,
342 which is not the case for the aforementioned models. While some hydrologic models have a better
343 representation of the land surface processes (Noah-MP (Niu et al., 2011), VIC (Variable
344 Infiltration Capacity Model Macroscale Hydrologic Model) (Liang et al., 1994)), these models do
345 not have a detailed representation of the subsurface flows. Because the surface flow is important
346 in the region and it establishes the connection between the headwaters and the valleys, its good
347 representation is essential for projecting changes in hydrology. Compared to other integrated
348 hydrologic models (CATHY (Catchment Hydrology) (Bixio et al., 2002), MIKE-SHE (Abbott et
349 al., 1986)), ParFlow has the advantages of solving a two-dimensional kinematic flow equation that
350 is fully coupled to the Richards equation.

351 ParFlow is coupled to the Community Land Model (CLM) to solve the surface energy and
352 water balance, which enables interactions between the land surface and the lower atmosphere and
353 the calculation of key land surface processes governing the system hydrodynamics such as
354 evapotranspiration, infiltration, and snow dynamics. CLM models the thermal processes by closing
355 the energy balance at the land surface given by:

$$356 \quad R_n(\theta) = LE(\theta) + H(\theta) + G(\theta) \quad (4)$$

357 Where $\theta = \phi S_w$ is the soil moisture, R_n is the net radiation at the land surface (E/LT) a
358 balance between the shortwave (also called solar) and longwave radiation, LE is the latent heat
359 flux (E/LT) which captures the energy required to change the phase of water to or from vapor, H
360 is the sensible heat flux (E/LT) and G is the ground heat flux (E/LT).

361 More information about the coupling between ParFlow and CLM can be found in Maxwell
362 & Miller, (2005). CLM uses the following outputs of the VR-CESM model at 3-hourly resolution

363 to solve the energy balance at the land surface: precipitation, air temperature, specific humidity,
364 atmospheric pressure, north/south and east/west wind speed, and shortwave and longwave wave
365 radiation.

366 We constructed a high-resolution model of the Cosumnes watershed with a horizontal
367 discretization of 200 m and vertical discretization that varies from 10 cm at the land surface to 30
368 m at the bottom of the domain. The model has 8 layers, the first 4 layers represent the soil layers
369 and the other four the deeper subsurface. The total thickness of the domain is 80 m to ensure
370 appropriate representation of water table dynamics. Observed water table depths (as measured at
371 several wells located in the Central Valley portion of the domain) vary between approximately 50
372 m and the land surface through a multi-year time period (Maina et al., 2020a). Therefore, to be
373 conservative for imposing the lower boundary layer, anything below 80 m is expected to remain
374 fully saturated. The resulting model comprises approximately 1.4 million active cells and was
375 solved using 320 cores in a high-performance computing environment. The Cosumnes watershed
376 is bounded by the American and Mokelumne rivers. We, therefore, impose weekly varying values
377 of Dirichlet boundary conditions along these borders to reflect the observed changes of river stage.
378 The eastern part of the watershed corresponding to the upper limit in the Sierra Nevada is modeled
379 as a no-flow (i.e., Neumann) boundary condition. Hydrodynamic parameters required to solve the
380 surface and subsurface flows (e.g., hydraulic conductivity, specific storage, porosity, and
381 van Genuchten parameters) are derived from a regional geological map (Geologic Map of
382 California, 2015; Jennings et al., 1977) and a literature review of previous studies (Faunt et al.,
383 2010; Faunt and Geological Survey (U.S.), 2009; Gilbert and Maxwell, 2017; Welch and Allen,
384 2014). We use the 2011 National Land Cover Database (NLCD) map (Homer et al., 2015) to
385 define land use and land cover required by CLM. We further delineate specific croplands (notably

386 alfalfa, vineyards, and pasture) in the Central Valley by using the agricultural maps provided by
387 the National Agricultural Statistics Service (NASS) of the US Department of
388 Agriculture's (USDA) Cropland Data Layer (CDL) (Boryan et al., 2011). Vegetation parameters
389 are defined by the International Geosphere-Biosphere Programme (IGBP) database (IGBP, 2018).
390 A complete description of the model parameterization can be found in [appendix B and more details](#)
391 [in Maina et al. \(2020a\)](#). The model has been extensively calibrated and validated using various
392 datasets, including remotely sensed data and ground measurements, which are however very sparse
393 in the area. Model validation which consists in comparing both surface and subsurface
394 hydrodynamics (groundwater and river stages) and land surface processes was performed over a
395 period [of three years](#) that includes extremely dry and wet [water years](#) ([Appendix C](#)). [We](#)
396 [specifically compared simulated and measured river stages at three stations located in the Sierra](#)
397 [Nevada headwater, foothill, and the Central Valley. The annual averages absolute differences](#)
398 [between measurements and simulations were between 0.4 and 0.8 m. We selected four wells in the](#)
399 [Cosumnes watershed based on their availability of data to compare measured and simulated](#)
400 [groundwater levels. These wells are sparsely distributed in the Central Valley. The absolute](#)
401 [differences observed and simulated groundwater levels vary between 0.47 to 3.73 m. The highest](#)
402 [absolute differences were attributed to the lack of a best estimation of groundwater pumping rates](#)
403 [in the region. Nonetheless,](#) the reasonable agreement between observations and simulated variables
404 has allowed us to conclude that the model can capture these extreme dynamics. [We rely on remote](#)
405 [sensing data to assess the ability of our model to simulate key land surface processes](#)
406 (evapotranspiration, soil moisture, and snow dynamics). [We compared the simulated SWE to](#)
407 [SNODAS \(The National Weather Service's Snow Data Assimilation, National Operational](#)
408 [Hydrologic Remote Sensing Center, 2004\) and a SWE reanalysis by Bair et al., \(2016\). Our](#)

Deleted:

Deleted: T

Deleted: Annual average differences between simulated and measured river stages and groundwater levels vary between 0.4 and 0.8 m and 0.47 to 3.73 m respectively.

Deleted: K

415 [comparisons indicated that the absolute differences between our SWE values and these data were](#)
416 [equal to 3 mm on average. Moreover, the simulated key parameters controlling the snow dynamics](#)
417 [such as peak snow and timing of snow ablation were also in agreement with remotely sensed data](#)
418 [for both dry and wet years \(Appendix C\). Absolute differences between the simulated ET and the](#)
419 [remotely sensed ET from METRIC \(Mapping Evapotranspiration at High Resolution with](#)
420 [Internalized Calibration, Allen et al., 2007\) were equal to 0.036 mm/s while the differences](#)
421 [between the simulated soil moisture and the SMAP \(Soil Moisture Active Passive, SMAP, 2015\)](#)
422 [soil moisture were 0.2. More details about model calibration and validation can be found in](#)
423 [Appendix C and](#) previous publications (Maina et al., 2020a, Maina et al., 2020b; Maina and Siirila-
424 Woodburn, 2020c). The model has also been successfully used in recent investigations of post-
425 wildfire and climate extremes hydrologic conditions and to assess the role of meteorological
426 forcing scale on simulated watershed dynamics (Maina et al., 2020a, b; Maina and Siirila-
427 Woodburn, 2020c). Initial conditions for pressure-head were obtained by a spin-up procedure
428 using the forcing of the historical median WY. We recursively simulated the historical median
429 WY forcing until the differences of storage at the end of the WY were less than 1%, indicating
430 convergence. This pressure head field is then used as the initial condition for each of the five WYs
431 of interest (i.e. the EoC wet, EoC dry, historic wet, historic dry, EoC median). Though we
432 acknowledge land cover alterations are expected to occur by the EoC (either naturally or
433 anthropogenically), in this work we assume that the vegetation remains constant for both historical
434 and EoC simulations for simplicity. Although outside of the scope of this work, future studies will
435 investigate the impacts of an evolved land use/land cover, vegetation physiology, and resilience
436 strategies to manage water resources. Further, while the Central Valley of California hosts
437 intensive agriculture that is reliant on groundwater pumping for irrigation, we didn't incorporate

Deleted: he National Weather Service's Snow Data Assimilation (SNODAS) (National Operational Hydrologic Remote Sensing Center, 2004) and were also in agreement with remotely sensed values. For example, annual average differences between the measured and simulated snow water equivalent, soil moisture, and evapotranspiration are equal to 3 mm, 0.2, and 0.036 mm/s respectively. Simulated key parameters controlling the snow dynamics such as peak snow and timing of snow ablation were also in agreement with remotely sensed data for both dry and wet years.

448 pumping and irrigation in our model configuration. We did this with the assumption that
 449 groundwater pumping rates may substantially change in the future due to new demands, policies,
 450 regulations, and changes in land cover and land use and aim to provide an estimate of the natural
 451 hydrologic system response to climate change.

452

453 2.3. Analysis of EoC hydrodynamics

454 To investigate how the EoC climate extremes affect water storages, we investigate five
 455 hydrologic variables: Snow Water Equivalent (*SWE*), Evapotranspiration (*ET*), Pressure-head (ψ)
 456 distributions, and surface and subsurface water storage. Total groundwater (GW) storage is given
 457 by:

$$458 \quad Storage_{GW} = \sum_{i=1}^{n_{GW}} \Delta x_i \times \Delta y_i \times \Delta z_i \times \psi_i \times \left(\frac{S_{s_i}}{\phi_i} \right) \quad (5)$$

459 where n_{GW} is the total number of subsurface saturated cells (-), Δx_i and Δy_i are cell discretizations
 460 along the x and y directions (L), Δz_i is the discretization along the vertical direction the cell (L),
 461 S_{s_i} is the specific storage associated with cell i , ψ_i the pressure-head, and ϕ_i is the porosity.

462 Total surface water (SW) storage which account for any water located at the land surface
 463 (i.e., any cell of the model with a pressure-head greater than 0) and includes river water or overland
 464 flow is calculated via:

$$465 \quad Storage_{SW} = \sum_{i=1}^{n_{SW}} \Delta x_i \times \Delta y_i \times \psi_i \quad (6)$$

466 where n_{SW} is the total number of cells with surface water i.e. with surface ψ greater than 0 (-), and
 467 i indicates the cell.

468 We compare each EoC WY simulation to its corresponding historical WY counterpart and
 469 both the historical and EoC medians. This allows us to assess how EoC extremes change relative

470 to what is currently considered an extreme condition as well as to “normal” in the relevant time.

471 Comparisons are shown as a percent change (*PC*) calculated using:

$$472 \quad PC_{i,t} = \frac{X_{projection_{i,t}} - X_{baseline_{i,t}}}{X_{baseline_{i,t}}} \times 100 \quad (3)$$

473 where *X* is the model output (*ET*, *SWE*, or ψ) at a given point in space (*i*) at a time (*t*), *baseline* is
474 the selected simulation (historical median, EoC median, or historical extreme), and *projection*
475 represents the simulation obtained with the EoC extreme WYs (dry or wet).

476

477 3. Results

478 In this section, we present a subset of the outputs from VR-CESM (precipitation and
479 temperature) to identify the extreme (dry and wet) and median WYs of interest. Changes in fluxes
480 and storages over the course of each WY, as well as the spatial variability of these changes in two
481 important periods of the WY (peak flow and baseflow) are also shown.

482

483 3.1. Selection of the median, dry, and wet WYs

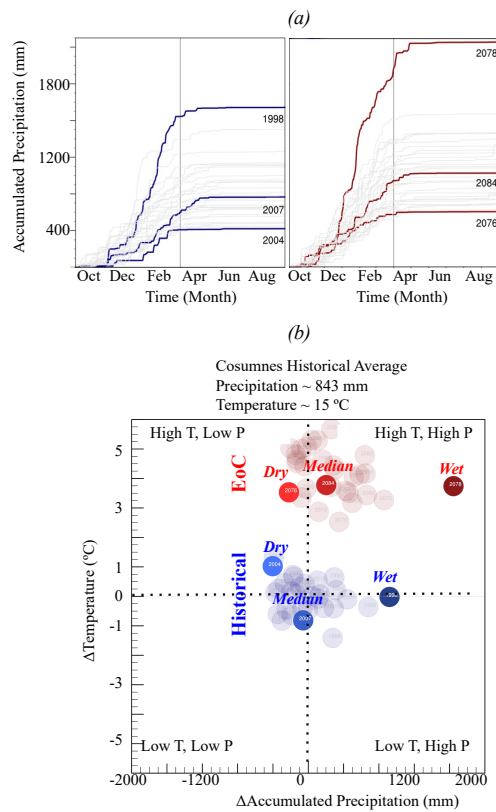
484 From the historical and EoC 30-year VR-CESM simulations we select the median, wettest,
485 and driest WYs for comparison (see Figure 3a). Overall, the future WYs are ~30% wetter than the
486 historical WYs (p-value ~0.006 for two-tailed t-test of equal average annual precipitation) in
487 addition to being ~4.6°C warmer. Precipitation and temperature variances are mostly similar in the
488 historical and EoC simulations, though EoC minimum temperature may be more variable (p-value
489 ~0.059 for two-tailed f-test of equal variance in minimum temperature). On average the timing for
490 the start, length, and end of precipitation is similar, though EoC precipitation may be less variable
491 in its start time (p-value ~0.053 for f-test of equal variance in days to reach 5th percentile of annual

492 precipitation). In the climate model, there are no clear trends between the precipitation timing
493 metrics and total amount of precipitation.

494 The EoC median WY is much wetter than its historical counterpart, with about ~250 mm
495 more precipitation that begins approximately 1 week earlier and ends approximately 2 weeks
496 earlier in the year. The EoC wettest WY is much wetter than the historical wettest WY and is
497 characterized by 42% more precipitation. This is consistent with Allan et al. (2020), who suggest
498 a wetter future. The EoC wettest WY is 3.8°C warmer than the historical wettest WY and 4.6°C
499 warmer than the historical median WY, as the historical median WY is one of the coolest years in
500 the series. Precipitation occurs earlier in the EoC wet WY compared to the historical wet or median
501 WYs, with the 5th percentile of precipitation reached 12 days earlier in the EoC wettest WY than
502 either the wettest or median historical WYs. The duration of the EoC wettest WY precipitation
503 season (146 days) is between the historical wettest WY (133 days) and the historical median WY
504 (155 days).

505 The EoC dry WY is also much wetter than its historic counterpart; in fact, the EoC dry WY
506 is wetter than the seven driest historical WYs of the 30-year historical ensemble. Simulation of 30
507 random draws from two identical normal distributions, repeated 100,000 times, finds that the
508 lowest value in one is higher than the seven lowest values in the other only ~1.1% of the time (p-
509 value ~0.011). This statistical test reveals that this VR-CESM simulation suggests that future dry
510 years will be somewhat wetter than historical dry years. The EoC dry WY is only ~2.5°C warmer
511 than the historical dry WY. The divergence in temperature is smaller for the comparison of EoC
512 and historical WYs of the dry extremes as opposed to the wet extremes because the historical dry
513 WY is the second-warmest WY in the historical simulations, while the EoC dry WY is the third
514 coolest in the EoC simulations. Precipitation in the EoC dry WY starts particularly early, with the

515 5th percentile of annual precipitation reached by mid-October. This is much earlier than either the
 516 dry or median historical WYs, which don't reach that percentile of precipitation until mid-to-late-
 517 November. The historical dry WY also has a particularly short precipitation duration of only 97
 518 days, while the EoC dry WY has a 163-day precipitation duration, more similar to the median
 519 historical WY duration of 155 days.

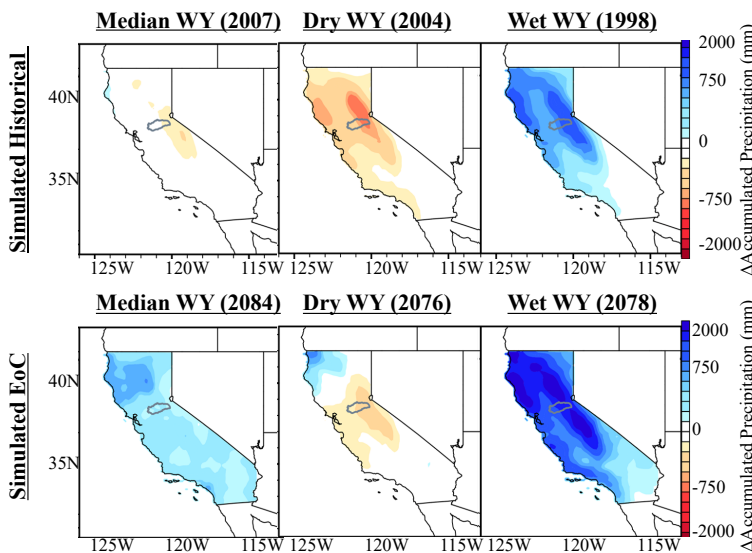


520
 521 Figure 3: (a) VR-CESM accumulated total precipitation for the historical and End of Century
 522 (EoC) simulations, and (b) quadrants for differences between each individual water year (WY)

523 and the historical average temperature and accumulated precipitation in the Cosumnes watershed.
524 The historical and EoC dry, median and wet WYs are indicated in blue and red, respectively.
525

526 Figure 4 shows the spatial distribution of accumulated precipitation anomalies across
527 California. These anomalies are computed for each of the six identified WYs relative to the
528 climatological average (the 30-year historical mean). These spatial plots provide context for the
529 changes modeled in the Cosumnes watershed relative to broader precipitation changes California-
530 wide. As in the Cosumnes, California-wide EoC dry, median, and wet WYs are all characterized
531 by higher precipitation totals than their historical counterparts. Importantly, the EoC wet WY is a
532 true outlier not only in the Cosumnes but across California too. California lies at an important
533 large-scale circulation transition, namely semi-permanent high-pressure systems associated with
534 the Hadley circulation. Therefore, how climate change alters the atmospheric dynamics over
535 California, or more specifically how far northward storm-tracks may shift, remains uncertain and
536 depends on climate model choice. This has led to papers that claim the future of California will be
537 wet across a range of climate models (e.g., Neelin et al, 2013; Swain et al., 2013; Gershunov et al.,
538 2019; Rhoades et al., 2020b; Persad et al., 2020) and, for select climate models, that it could be
539 drier. Notably, these studies highlight an asymmetric response in the frequency of wet versus dry
540 WYs (i.e., anomalously wet WYs increase in frequency much more in the future than anomalously
541 dry WYs). Many of the aforementioned studies also highlight that in anomalously wet WYs
542 extreme precipitation events (e.g., atmospheric rivers) will occur with greater intensity and
543 frequency and largely drive changes in WY precipitation totals (which is shown in our VR-CESM
544 simulations for California in more detail in Rhoades et al., 2020b). Given these complexities and
545 others such as consideration for how dynamical and thermodynamical effects of climate change

546 may interact with one another to offset or amplify extreme precipitation events (Payne et al., 2020),
 547 the hypothesis that global warming will result in a climate where the “wet gets wetter and dry gets
 548 drier” may be too simplistic of an assumption for California. Rhoades et al., (2020b) shows
 549 quantitatively that the increases in precipitation observed in the VR-CESM outputs are due to a
 550 greater number of intense atmospheric river events that occur more regularly back-to-back, which
 551 was recently corroborated by Rhoades et al. (2021) using uniform-high-resolution CESM
 552 simulations at different warming scenarios, and that atmospheric river precipitation totals increase
 553 at a much larger rate (+53%/K) than non-AR precipitation totals (+1.4%/K), which agrees with
 554 findings made in other studies such as Gershunov et al. (2019).

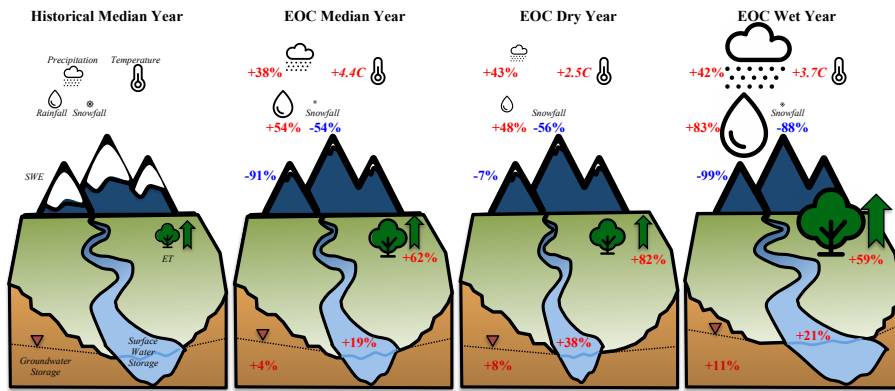


555
 556 Figure 4: Precipitation spatial distributions of the dry, median, and wet water years (WY) for the
 557 30-year historical and EoC simulations relative to the climatological average (derived from the 30-
 558 year historical mean)

559

560 **3.2. Changes in annual watershed-integrated fluxes and storages**

561 Figure 5 illustrates the annual changes in the integrated hydrologic budget of the Cosumnes
562 watershed for the EoC WYs (i.e., median, dry, and wet) compared to the historical median WY.
563 The EoC median WY compared to the historical median WY has 38% more precipitation and the
564 temperature is 4.4°C higher. Further, the precipitation phase also shifts with an increase in rainfall
565 (54%) and a decrease in snowfall (-54%). This results in a significant decrease in *SWE* (-91%)
566 which is consistent with many other studies that have shown that increased temperatures due to
567 climate change will lead to low-to-no snow conditions (Berghuijs et al., 2014; Cayan et al., 2008;
568 Mote et al., 2005; Rhoades et al., 2018 a,b; Son & Tague, 2019). The increase in temperature and
569 precipitation results in an increase in *ET* (62%), consistent with the findings of other recent studies
570 (e.g. McEvoy et al., 2020). Nevertheless, the larger amount of precipitation associated with the
571 EoC is enough to offset higher *ET* demand and recharge groundwater and surface water, which
572 experience an increase of 4% and 19% respectively. The EoC wet WY has similar changes as the
573 EoC median WY when compared to the historical wet WY yet the magnitude of the increase in
574 surface (21%), and groundwater (11%) storages are higher due to more precipitation and higher
575 temperatures. The dry EoC WY is also characterized by higher precipitation (43%, the largest
576 increase) than its historical counterpart, this results in large increases in total groundwater (8%)
577 and surface water (38%) storages.



578

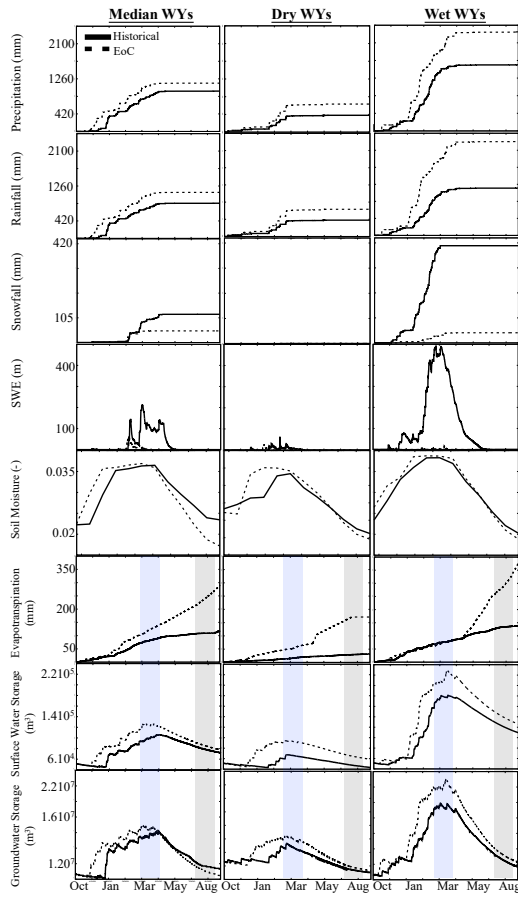
579 Figure 5: Annual percent changes in precipitation, rainfall, snowfall, temperature, *SWE*, *ET*,
 580 surface water, and groundwater storages in the EoC water years (WY) (i.e median, dry, and wet)
 581 at the watershed scale relative to their historical counterparts. Info-graphic size scaled to EoC
 582 conditions.

583

584 3.3. Temporal variation of watershed-integrated fluxes and storages

585 Understanding the annual changes at the watershed scale is important to broadly
 586 understand changes in the water budget in response to future climate extremes. However, a deeper
 587 understanding of the processes that drive these changes and the interactions from atmosphere-
 588 through-bedrock requires an analysis of their spatiotemporal variations as well. Figure 6 shows
 589 the temporal variations of each of the historical and EoC WY's integrated hydrologic budgets
 590 grouped by WY type (columns), with a top-down sequencing of hydrologic variables of interest in
 591 order from the atmosphere through subsurface (rows). This organization allows for the
 592 investigation of propagating impacts to be directly compared in time. In this section, we discuss
 593 historical vs EoC changes observed in each of the WY types (i.e., median, dry, and wet). Each WY
 594 shows unique hydrodynamic behaviors and changes compared to the historical conditions. The

595 median WY sheds light on how changes in the precipitation phase and increases in temperature
 596 and precipitation in the EoC will impact the hydrodynamics. The dry WYs allow comparing EoC
 597 and historical low-to-no snow conditions whereas assessing the hydrodynamics of the EoC wet
 598 WY provides a better understanding of how intense EoC precipitation along with the warm EoC
 599 climate will shape the hydrology.



600

601 Figure 6: Temporal variations of the total cumulative precipitation, rainfall, and snowfall at the
602 watershed scale, total *SWE* at the watershed scale, the average watershed values of soil moisture,
603 the cumulative watershed *ET*, and the total surface water, and groundwater storages at the
604 watershed scale associated with the six historical and EoC Water Years (WY). The blue area
605 indicates the selected peak flow period while the gray area corresponds to the selected baseflow
606 conditions for the spatial distribution analyses.

607

608 **3.3.1. Median water years**

609 As indicated in section 3.1, the EoC median WY has more precipitation than the historical
610 median WY. The EoC precipitation comes mainly as rain due to the warmer temperatures of the
611 EoC and includes virtually no snowfall from late-winter to early-spring. This precipitation phase-
612 change combined with the earlier snowfall cessation date in the WY results in minimal and even
613 non-existent *SWE* in the Cosumnes watershed for much of the WY, a significant change compared
614 to historic conditions. EoC peak *SWE* occurs in February in contrast to the historical peak *SWE*,
615 which occurs in April. Due to the watershed's relatively low elevation, snow accumulates only in
616 the upper part of the Cosumnes watershed (~10% of the total watershed area). Only areas located
617 in the highest elevations (> 2000 m), such as the eastern limit of the watershed, show any *SWE* in
618 the EoC simulations whereas in the historical WYs we observed *SWE* as low as 1000 m.

619 The decrease in snow and the increase in rain along with an earlier onset of seasonal
620 precipitation directly impacts soil moisture, which sees an early increase with a slightly higher
621 peak than historical. As more water is available earlier in the EoC, the *ET* demand from increased
622 temperatures is met until substantially higher summer temperatures increase *ET* at a much faster

623 rate than the historical WY. The high EoC *ET* and the lack of snowmelt cause the soil to rapidly
624 dry from late-spring through late-summer.

625 Because of the marked increase in total precipitation and shift from snow to rain in the EoC
626 simulations, surface water storage generally increases throughout the WY. This is consistent with
627 previous studies (Gleick, 1987; He et al., 2019; Maurer, 2007; Safeeq et al., 2014; Son & Tague,
628 2019; Vicuna & Dracup, 2007; Vicuna et al., 2007). Surface water storage increases in early
629 November in the EoC simulations while in the historical simulations this increase occurs in
630 January. Similar to the earlier peak *SWE* and soil moisture, the peak surface water storage in the
631 EoC is also earlier (January through February) compared to the historical period (March through
632 April). This late-season surface water storage remains larger because the accumulated precipitation
633 is large enough to overcome the increased *ET* in a warmer climate. Similar to surface water storage,
634 groundwater storage increases earlier and peaks at a larger amount than the historical WY.
635 However, in contrast to the surface water storage, the groundwater storage during baseflow
636 conditions is lower in the median EoC compared to the median historical year. This decrease in
637 groundwater during baseflow conditions is due to the lack of snowmelt and higher EoC *ET*. In
638 late-spring and summer in the EoC, groundwater keeps depleting through *ET* and is not recharged
639 by snowmelt through surface and subsurface flows from the Sierra Nevada as in the historical
640 period. This may indicate that compared to surface water storages, groundwater storage may be
641 more sensitive to EoC hydroclimatic changes (which are multi-fold, and in this case include an
642 increase in precipitation, a transition from snow to rain, and higher *ET*). One way to quantitatively
643 measure this sensitivity is to compare the seasonal change in water storage between peak and
644 baseflow conditions. Historically, changes between peak and baseflow conditions (i.e., the amount
645 of water lost between peak and base flow) resulted in moderate seasonal changes in groundwater

646 storage (30%) and surface water storage (32%). The EoC simulations reveal larger seasonal
647 variation for groundwater and surface water storage (40% and 37% decreases, respectively).
648 Groundwater in the Cosumnes Watershed is mainly recharged in the headwaters and stored in the
649 Central Valley. Therefore, these Central Valley aquifers experience earlier and larger increases in
650 storage which lead to more water available to *ET* and therefore aquifer depletion. A deeper
651 understanding of this phenomenon requires an analysis of the spatial patterns of these changes
652 which is performed later on in this study.

653

654 **3.3.2. Dry water years**

655 All EoC WYs are characterized by higher precipitation in the form of rainfall compared to
656 their historical counterparts. The historical dry WY has ~43% less total precipitation than the EoC
657 dry WY. However, we note that for the EoC dry WY the decrease in snowfall is less drastic than
658 the median or wet EoC years. This is because the historically driest WY is significantly warmer
659 than the historical average WY, and therefore already has a smaller snowpack, 94% lower than the
660 historical median WY. The EoC dry WY *SWE* also accumulates two months earlier than the
661 historical *SWE*. Because the differences in *SWE* between the dry WYs are smaller than the
662 differences in *SWE* between the median WYs (7% versus 91%), we can deduce that the early and
663 larger rise in soil moisture in the EoC dry WY is mostly due to an earlier and larger amount of
664 rainfall. The higher soil moisture and EoC temperatures result in higher *ET* throughout the WY
665 compared to the historical WY. This *ET* results in lower soil moisture by the end of the summer,
666 similar to the median WY. In addition, surface water storage peaks earlier and at a larger amount
667 compared to the historical WY. The surface water storage in the EoC remains higher throughout
668 the WY compared to its historical counterpart despite this higher *ET* due to the low precipitation

669 associated with the historical dry WY. We further note that the difference in surface water storage
670 during baseflow conditions between the two dry WYs is higher than the difference between the
671 two median WYs. The groundwater recharge starts two months earlier in the EoC driest WY
672 compared to the historical driest WY due to the changes in timing and magnitude of precipitation.
673 However, it is interesting to note that groundwater storage during baseflow conditions in the EoC
674 WY is nearly equal to the historical WY (within 3%). Thus, although more water enters the EoC
675 dry WY system through greater precipitation, it eventually exits by the end of the WY and no
676 considerable net gains to groundwater are observed. This significant reduction in groundwater
677 storage from late-winter to end-of-summer is a result of the much larger EoC *ET* and highlights
678 the dynamic nature of the EoC dry year watershed interactions. Also similar to the median WY,
679 dry WY seasonal decreases in EoC storage are more pronounced in the groundwater signal (36%)
680 than in the surface water signal (33%). We further note that the decreases in groundwater and
681 surface water storages are, as in the median WY, larger (+8%) than the historical decreases.

682

683 **3.3.3. Wet water years**

684 The EoC wet WY is significantly wetter than all other WYs. Yet, unlike the historical WY,
685 the precipitation largely comes as rain, as shown by the low-to-no snowfall and *SWE* totals (Figure
686 6). The difference in future versus contemporary wet WY *SWE* (99%) is larger than the differences
687 between the median and the dry WYs (91%). As in other WYs, soil moisture increases earlier
688 compared to the historical wet WY. A greater water availability enables the system to meet the
689 high EoC *ET* demand. Hence, *ET* in the EoC wettest year remains higher than the historical wettest
690 year *ET* throughout the WY. However, the increase in *ET*, combined with the lack of snowmelt
691 that can buffer and recharge soil moisture in spring, leads to less soil moisture at the end of the

692 WY compared with the historical WY. Further, surface water storage increases earlier and at a
693 much faster rate in the EoC WY compared to the historical WY. This is mirrored in the
694 groundwater storages. As in the other EoC simulations, when compared to the historical
695 counterpart the EoC wettest year shows a sharper decline in seasonal above and below ground
696 water storage changes (occurring between peak flow and baseflow). Groundwater storage
697 decreases 47% in the EoC between peak flow and baseflow, whereas only a 41% decrease occurs
698 in the historical wet WY. Similarly, surface water storage decreases 44% in the EoC whereas only
699 a 41% decrease occurs in the historical wet WY.

700

701 **3.4. Spatial patterns of the changes in fluxes and pressure-heads**

702 **3.4.1. Median water years**

703 To provide a deeper understanding of how the changes in precipitation timing, magnitude,
704 and phase affect the land surface processes and surface and subsurface hydrodynamic responses,
705 we assess the spatial patterns of these changes during two key periods in the WY, peak flow and
706 baseflow. Figure 7 shows the percent changes in *ET*, surface water pressure-heads, and subsurface
707 pressure-heads (i.e., pressure-heads of the model bottom layer) in the EoC median WY compared
708 to the historical median WY during peak flow and baseflow conditions (see the time frames in
709 Figure 6). Regions in red correspond to areas with smaller fluxes or pressure-heads in the EoC
710 compared to the historical ones, whereas regions in blue correspond to areas with larger fluxes or
711 pressure-heads in the EoC compared to the historical median WY. We study peak flow and
712 baseflow conditions because the analysis of the temporal variations of fluxes and storages has
713 shown that these two periods are characterized by different trends and represent the key periods in
714 understanding the hydrologic responses to the EoC extreme climate.

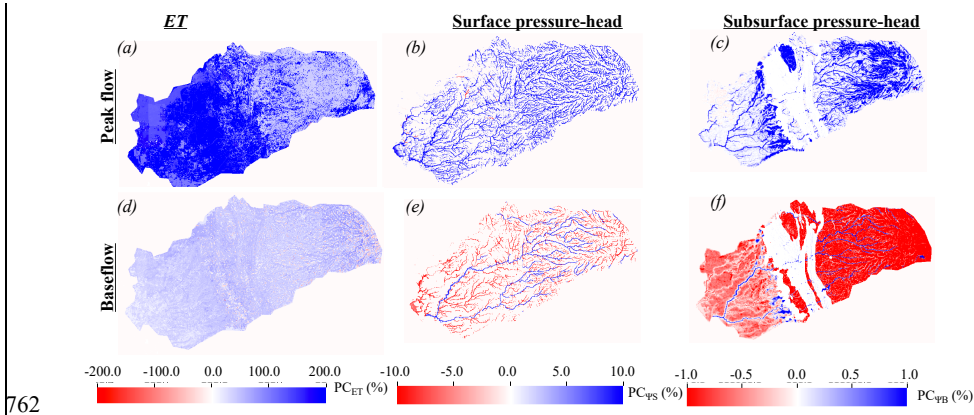
715 Relative to the historical median WY, during peak flow the EoC median WY is
716 characterized by an increased *ET* across the majority of the watershed, especially in the Central
717 Valley, and larger surface water and subsurface pressure-heads (Figure 7a-c). *ET* increases in the
718 EoC both because of the increase in water availability and increased evaporative demand, as
719 discussed in the previous section (3.3.1.). The increase in *ET* is non-uniform across the watershed
720 because of the heterogeneity of the landscape's topographical gradients, land-surface cover, and
721 subsurface geological conditions. The Central Valley is characterized by a large increase in *ET*
722 compared to the Sierra Nevada, and the patterns of *ET* in the Central Valley are also more
723 homogeneous, a resultant of the geological characteristics of the area and the hydroclimate of the
724 watershed (i.e. where most of the precipitation falls over the Sierra Nevada but follows topographic
725 gradients downward into the valley where more recharge occurs). This leads to more water
726 available in the Central Valley compared to the Sierra Nevada characterized by less permeable
727 rocks. In addition, as most of the *ET* in the Central Valley comes from evaporation due to the high
728 temperatures of the EoC (not shown here), the increase in evaporation is higher in the Central
729 Valley due to its aquifers characterized by a high permeability (Maina and Siirila-Woodburn,
730 2020) and the availability of water.

731 Surface and subsurface pressure heads both show general increases during the EoC peak
732 flow, yet these maps reveal that unlike *ET* the pressure head (and therefore storage) of water is
733 very heterogeneous in space. For example, in the Sierra Nevada, we observe an increase in
734 subsurface pressure-head (Figure 7c) only in some relatively permeable areas susceptible to
735 infiltration and recharge. Although the Central Valley aquifers are more permeable and
736 geologically less heterogeneous than the Sierra Nevada (as defined in the model), the changes in
737 subsurface pressure-head in the Central Valley are heterogeneous. This is because the recharge of

738 the Central Valley aquifers is dependent on the subsurface and surface flows from the headwater
739 (i.e., connectivity to the headwater). In other words, only areas of the Central Valley that are
740 subject to stronger connectivity with the headwaters see an increase in subsurface pressure-head
741 in the EoC, likely because they are more regularly recharged by the headwaters through surface
742 and subsurface flows from these areas, a recharge that buffers the water depletion through *ET*.
743 These are mostly the areas located close to the streams where there is an exchange between the
744 subsurface and the surface and the Sierra Nevada foothills (in the alluvium 3 area, see Figure 1).

745 Relative to its historical counterpart, the EoC median WY is characterized by high *ET*
746 during baseflow conditions though less than during peak flow conditions. (Figure 7d). We observe
747 larger surface water pressure-heads in higher-order streams whereas surface water pressure-heads
748 decrease in the EoC in the majority of the low-order, ephemeral streams (Figure 7e). This
749 opposition of spatial pattern trends, resulting in more water in the main river channels, and less in
750 the smaller streams, occurs for several reasons. First, peak flow occurs earlier in the EoC and is
751 more rainfed, so that the ephemeral streams drain earlier in the EoC compared to in the historical
752 period. This sustained and longer duration of draining increases the surface water pressure-head
753 along the main river channels and is due to the contribution of the subsurface in the headwaters.
754 This contribution is also higher in the EoC due to larger amounts of precipitation. The trends along
755 the main river channel are also evident in the subsurface pressure-head maps (Figure 7f). Because
756 the surface water is larger along the main channels, the subsurface pressure-heads are also larger
757 here due to the interconnection between the subsurface and the surface (Figure 7f). However, in
758 general, subsurface pressure-heads decrease elsewhere in the EoC during baseflow because of the
759 lack of snowmelt and the higher *ET* demand. This result highlights the spatiotemporal complexity

760 of an expected watershed's response to changes in climate (shown here to be bi-directional), and
761 how factors such as river proximity may be crucial for consideration.



762
763 Figure 7: Comparisons between EoC median water year (WY) and the historical median WY peak
764 flow and baseflow spatial distributions of percent changes in ET (PC_{ET}), surface water (PC_{pS}) and
765 subsurface (PC_{pB}) pressure-heads. Regions in red correspond to areas with smaller fluxes or
766 pressure-heads in the EoC compared to the historical ones, whereas regions in blue correspond to
767 areas with larger fluxes or pressure-heads in the EoC compared to the historical WY.

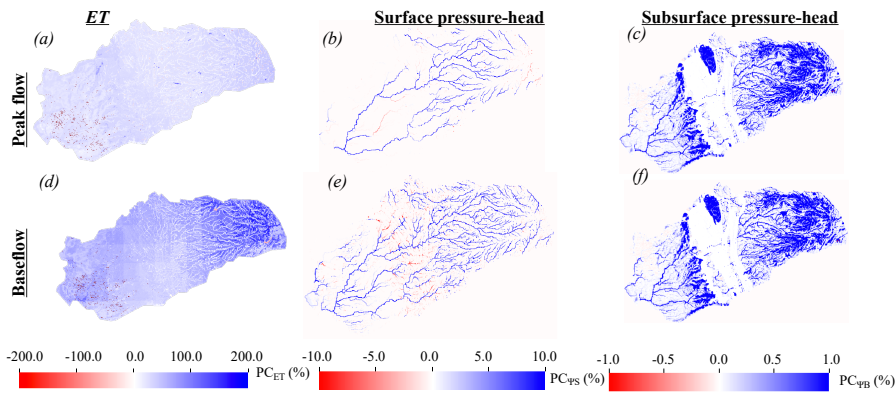
768

769 3.4.2. Dry water years

770 Figure 8 illustrates the percent changes in ET , surface water, and subsurface pressure-heads
771 in the EoC dry WY compared to the historical dry WY during peak flow and baseflow conditions.
772 During peak flow conditions, the EoC dry WY has larger ET , surface, and subsurface pressure-
773 heads than the historical dry WY (Figure 8a-c). ET is larger in this EoC dry WY not only because
774 it is hotter, but also because there is more precipitation, as noted previously. Increases in surface
775 pressure-heads are non-uniform across the domain. For example, surface water does not increase

776 in high elevation areas (i.e. elevation > 2000m) in the EoC dry WY because the change in the
777 precipitation phase is not significant. The main difference between the EoC and the historical dry
778 WY is the amount of the water flowing down gradient, which is higher in the EoC, hence the
779 surface water in the EoC becomes higher downstream. The increase in subsurface pressure-heads
780 in the EoC dry WY during peak flow conditions is heterogeneous with patterns similar to the
781 changes in subsurface pressure-heads associated with the EoC median WY.

782 During baseflow conditions, even though *ET* increases in the EoC driest WY relative to
783 the historical driest WY, surface, and subsurface pressure-heads also generally increase (Figure
784 8d-f). Given wetter conditions in the driest EoC WY, first-order streams are more pronounced. A
785 few low-order streams have less surface water in the EoC when compared to the historical dry
786 WY, similar to the results of the median WYs (see section 3.4.2). Subsurface pressure-head is
787 generally larger in areas subject to strong connectivity with the headwaters (i.e., receiving more
788 water from the headwaters through subsurface and surface flows) in the EoC dry WY relative to
789 the historical dry WY, with some regions experiencing no change from the historical conditions.
790 This suggests that the larger amount of precipitation associated with the EoC dry WY is sufficient
791 to supply enough water to account for high *ET* demands and recharge the groundwater.



792

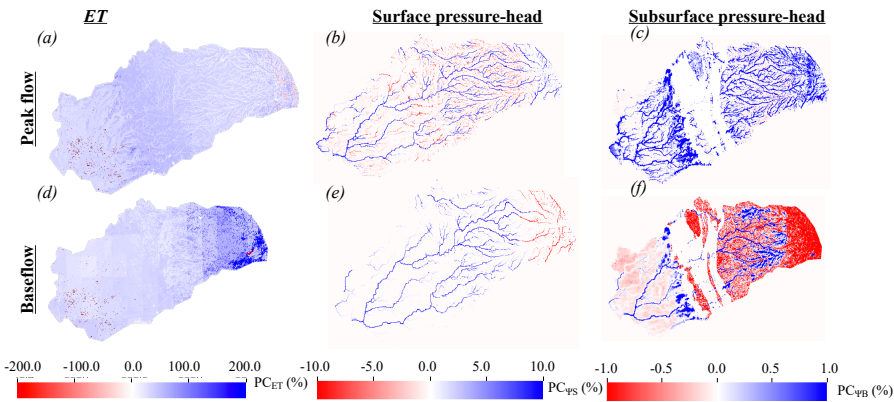
793 Figure 8: Comparisons between EoC dry water year (WY) and the historical dry WY peak flow
 794 and baseflow spatial distributions of percent changes in ET (PC_{ET}), surface water (PC_{pS}) and
 795 subsurface (PC_{pB}) pressure-heads. Regions in red correspond to areas with smaller fluxes or
 796 pressure-heads in the EoC compared to the historical ones, whereas regions in blue correspond to
 797 areas with larger fluxes or pressure-heads in the EoC compared to the historical WY.

798

799 **3.4.3. Wet water years**

800 Figure 9 shows the percent changes in ET , surface water, and subsurface pressure-heads in
 801 the EoC wet WY compared to the historical wet WY during peak flow and baseflow conditions.
 802 During peak flow, the EoC wet WY is characterized by larger ET and subsurface pressure-heads
 803 relative to the historical wet WY and a more heterogeneous mixture of regions with both higher
 804 and lower surface water conditions throughout the catchment (Figure 9 a-c). Analogous to other
 805 WYs at EoC, the surface water pressure-head increases (decreases) are apparent in larger-order
 806 (smaller order) streams, both in the Sierra Nevada and in the Central Valley. In the wettest WY,
 807 this occurs for several reasons. First, the larger volume of precipitation, plus seasonal shifts in

808 precipitation timing result in the filling of the higher-order streams and depletion of the lower-
 809 order streams during peak flow. Second, in the historical wet WY, a significantly greater amount
 810 of snowpack is present in the Sierra Nevada in the upper elevation of the headwaters, allowing for
 811 slower, steadier amounts of water that is released during the spring via snowmelt, and in turn,
 812 supporting low-order streams over a longer period of time. The latter effect is immediately visible
 813 in Figure 9e, where decreases in EoC surface pressure heads are visible in the headwaters, despite
 814 the watershed-total showing an increase in EoC surface water storage during baseflow (see Figure
 815 6). Similar to the two previous EoC WYs, the subsurface pressure-head increases are shown more
 816 distinctly in the Central Valley during peak flow, under the main river channels, and in the foothills
 817 during baseflow (see previous sections on the discussion of hydroclimatic and geologic impacts).



818
 819 Figure 9: Comparisons between EoC wet water year (WY) and the historical wet WY peak flow
 820 and baseflow spatial distributions of percent changes in ET (PC_{ET}), surface water (PC_{Ps}) and
 821 subsurface (PC_{Pb}) pressure-heads. Regions in red correspond to areas with smaller fluxes or
 822 pressure-heads in the EoC compared to the historical ones, whereas regions in blue correspond to
 823 areas with larger fluxes or pressure-heads in the EoC compared to the historical WY.

824

825 **4. Discussion**

826 **4.1 Comparison with previous studies**

827 Some of the results presented in this study are qualitatively in agreement with previous
828 studies yet provide important new insights. For example, Maurer & Duffy, (2005) used 10 global
829 climate models to predict, as in this study, an increase in winter flows with an earlier peak flow
830 timing in the WY and a decrease in summer flows. Maurer & Duffy show that mid-century
831 projected annual precipitation and streamflow increases of 7% and 13% (respectively). Although
832 our study focused on EoC projections, we found that compared to the historical median WY,
833 annual surface water will increase by 19% in the EoC median WY. Compared to their findings,
834 our work sheds light on how these changes in runoff will occur across the watershed based on its
835 physical characteristics and highlights that while runoff will increase in the EoC lower-order
836 streams mainly located in the Sierra Nevada will see a decrease due to the change in the
837 precipitation phase. Mallakpour et al., (2018) also had a similar finding in a study that shows that
838 future California streamflow is altered similarly to Maurer & Duffy, (2005) under both the RCP4.5
839 and RCP8.5 emissions scenarios, with RCP8.5 showing the highest changes during peak flow.
840 However, contrary to our work the authors mentioned that the annual changes in streamflow will
841 not be significant probably due to the compensation between increases in peak flow and decreases
842 in baseflow. This was likely shaped by the differences in climate and hydrologic models used to
843 derive these conclusions. Similar changes in streamflow were obtained by He et al., (2019) who
844 drove the hydrologic model VIC with 10 global climate models to understand potential changes in
845 runoff in California due to climate change. Hydrologic changes computed from the 10 global
846 climate models were consistent and robust and showed an increase of around 10% in annual

847 streamflow by the late century, a percentage similar to what has been found in this study. The
848 authors mentioned that watershed characteristics such as geology, topography, and land cover
849 strongly impact the hydrologic response to climate change. Relationships between watershed
850 characteristics (e.g., physiographic parameters) and its responses to climate change were further
851 explored by Son & Tague, (2019) who highlighted that because vegetation and subsurface geology
852 control both water availability and energy demand, they in turn influence watershed sensitivity to
853 a changing climate as shown in this study.

854 The increases in groundwater storage shown in this study are also in agreement with
855 Niraula et al., (2017) who used the hydrologic model VIC to show that groundwater recharge will
856 likely increase in the northern portion of the western United States in a changing climate. However,
857 contrary to their work that estimates changes in groundwater recharge over a large domain (i.e. the
858 western United States). In this work, we show that groundwater recharge decreases in the summer
859 in some areas due to the lack of snowmelt and high EoC *ET*. Increases in *ET* in response to global
860 warming were also documented by Pascolini-Campbell et al., (2021) who showed a 10% increase
861 in global *ET* from 2003 to 2019.

862 An advantage of our approach is a more explicit estimate of spatiotemporal changes in
863 groundwater-surface water feedbacks because Parflow-CLM physically solves the transfer and
864 movement of water from the bedrock to the canopy. Additionally, the aforementioned studies used
865 different emission scenarios and models to project changes in hydrology, nonetheless, their results
866 have shown that the directions of the observed changes are consistent across models and emission
867 scenarios and only the magnitude of these changes is uncertain. Hence, the trends observed in this
868 study using a single model and emission scenario likely represent the trends we would observe
869 using different models and scenarios. While our results show similar patterns and changes, our

870 study provides a much finer-grained perspective on the sensitivity of a watershed to changes in
871 climate extremes based on its subsurface geology, topography, and land cover. It also highlights
872 that the spatiotemporal analyses of these changes may reveal different trends than if only assessed
873 as annual changes. Understanding these localized changes and sensitivities is critical and has
874 practical implications for water management.

875

876 **4.2 Implications for water resources management**

877 Because our work provides a better understanding of the spatiotemporal changes in
878 hydrodynamics in response to future extremes, our findings also have important implications for
879 water resources in California. While previous work more broadly focused on how temperature
880 increases will alter the precipitation phase and reduce seasonal snowpack and increase winter
881 runoff, this work brings new physical and more granular insights into how watersheds may respond
882 to climate extremes. In particular, both wet and dry WYs in the future experience increased
883 precipitation. As such, even in future dry WYs, water managers and stakeholders may need to
884 prepare more for large precipitation events that may increase the possibility of flooding and require
885 new infrastructure management strategies. For example, in a future where WYs are generally
886 wetter, having alternatives for water supply during periods of sustained drought could be less
887 important. However, as we show in this paper, shifts in precipitation timing, phase, and magnitude
888 have cascading impacts on soil moisture profiles and *ET* withdrawals, which subsequently impact
889 discharge and groundwater dynamics. Future shifts in water availability earlier in the year, as well
890 as more dynamic transitions between peak and baseflow conditions (as quantified here), may
891 impose stresses on water distribution, especially those systems already under scrutiny (e.g. those
892 resources over-allocated or facing environmental degradation).

893 In addition, while these projections show increases in surface water and groundwater
894 storages at watershed-scale, our results also highlight important localized spatiotemporal changes
895 across a watershed, where the assumption of water storage increase does not necessarily hold in
896 all geographic locations (e.g., areas that are not close to the river in the Central Valley). Our study
897 also shows that the decreases in groundwater storage in the Central Valley aquifers are more
898 significant than the decreases in surface water storage during baseflow conditions. This may call
899 for new conveyance infrastructure that can move water from the relatively wetter areas to the drier
900 areas and/or where infiltration can more readily occur. The latter suggests solutions such as
901 Managed Aquifer Recharge (MAR) could become an increasingly important climate change
902 adaptation. Finally, our study also highlights that lower-order streams will likely become more
903 ephemeral in the EoC due to flashier runoff and higher evaporative demand, such conditions will
904 have important implications for fish spawning and ecosystem nutrient cycling. Although our
905 results are embedded with uncertainties and are based on a single projection and model, they do
906 highlight the need for a revisitation of current water management strategies. Further studies using
907 different climate and land-use scenarios and models of varying complexity and resolution could
908 help build more confidence and provide more information in defining how future water
909 management strategies would need to change to be more resilient to more extreme WYs in the
910 future.

911

912 **4.3 Study limitations**

913 This study combines novel climate and hydrologic simulations that provide both
914 advantages and disadvantages compared with previous work (He et al., 2019; Maurer & Duffy,
915 2005; Niraula et al., 2017; M. Safeeq et al., 2014; Son & Tague, 2019). We note several of these

916 disadvantages below. In the integrated hydrologic model, the subsurface geology and land cover
917 characterization has inherent and, in some cases, irreducible uncertainty. This study uses
918 hydrodynamic parameters as defined by Maina et al. (2020a), which assumes that the subsurface
919 hydrodynamics from the Sierra Nevada to the Central Valley is almost completely hydrologically
920 separated except through overland flow. However, it is not clear whether fractures or other
921 macrostructures may drive more surface and subsurface flows from the headwaters to the Central
922 Valley aquifers. In addition, we use the historical land surface cover map when simulating the
923 EoC. Since vegetation will dynamically respond to a changing climate, the land surface cover used
924 in the EoC simulations may be unrealistic and may influence, for example, *ET* and/or soil moisture.
925 For example, it has been shown that the stomatal resistance of plants will change due to rising CO₂
926 with important implications for both the water and energy balance (Lemordant et al., 2018; Milly
927 & Dunne, 2017). Yet, our use of historical land surface cover does have the advantage of isolating
928 changes in fluxes associated with climate change alone and could be compared in future work with
929 additional simulations that account for both changes in the land surface and climate. Future studies
930 will assess the impact of changes in vegetation physiology and land surface cover on watershed
931 hydrodynamics. In this study, we did not include the impacts of anthropogenic activities such as
932 pumping and irrigation due to the uncertainties in predicting these fluxes in EoC. While these
933 human interventions could substantially change the hydrologic system, our study isolates the
934 impacts of a changing climate on the natural system. Future studies can now estimate the impacts
935 of different pumping and irrigation scenarios at EoC that may further impact the hydrologic system
936 hydrodynamics in a changing climate and compare and contrast with this work. Last, although our
937 VR-CESM simulations represent a cutting-edge global climate model simulation (e.g., 28 km
938 regional grid-refinement, coupled atmosphere-land simulation with prescribed ocean conditions,

939 etc.), further work may be needed to evaluate how a more refined grid resolution impacts
940 atmospheric process representation over the Cosumnes watershed, particularly in the headwaters
941 (Maina et al., 2020b). We further acknowledge that the 30-year simulation may not be sufficient
942 to capture certain climate extremes (e.g., 1-in-50-year storm). Future studies, if computational
943 resources are available, will seek to explore how the use of a longer time period might influence
944 the identification of the most extreme dry and wet WYs from VR-CESM.

945

946 **5 Summary and Conclusions**

947 The effects of climate change are increasingly felt across many regions of the world,
948 especially in hydrologically sensitive regions with Mediterranean climates such as California.
949 Many studies over the years have been conducted to better understand the hydroclimate of the EoC
950 and its impacts on the hydrologic cycle. Previous studies have used a multitude of different models
951 at varying complexity and climate scenarios to highlight that the future climate has multiple
952 plausible outcomes. Most of these studies indicate warmer temperatures and precipitation that
953 mostly falls as rain instead of snow. For example, the state of California is projected to experience
954 more punctuated climate extremes coupled with a marked decrease in the Sierra Nevada snowpack
955 (Cayan et al., 2008; Gleick, 1987; Musselman, Molotch, et al., 2017; Rhoades, Ullrich, &
956 Zarzycki, 2018). Such drastic transitions have already started to shape the hydroclimate of
957 California. Faced with this new normal, it is becoming increasingly important to assess how the
958 integrated hydrologic cycle may respond to these perturbations and connect these responses more
959 directly to water resource management, particularly with modeling frameworks that can better
960 represent the interactions between the changing atmosphere and the surface and subsurface
961 hydrology.

962 In this work, we used state-of-the-art physics-based models at high resolutions for their
963 respective communities to project changes in meteorological conditions at the EoC and assess how
964 their combined effects influence watershed hydrology from the land surface to the deeper
965 subsurface. Importantly, our approach to couple a variable resolution Earth System Model and an
966 integrated hydrologic model allow for us to simulate hydro-meteorological conditions which are
967 jointly driven by thermodynamical and dynamical shifts in climate. We model the Cosumnes
968 watershed, which spans the Sierra Nevada and Central Valley and hosts one of the last rivers in
969 the state without a large dam, as a testbed to understand how climate drivers will impact water
970 resources in the EoC. We performed climate simulations over 30-year periods historically (1985-
971 2015) and at EoC (2070-2100) and identified the driest, median, and wettest WYs from those
972 simulations, which were then used as meteorological forcing for the hydrologic model. Our
973 coupled simulations project that, for the Cosumnes watershed, temperature and precipitation will
974 both increase by the EoC across all WY types (wettest, median, and driest). In addition,
975 precipitation is projected to fall earlier compared to historical conditions and mainly in the form
976 of rain. For the median and wet WYs the precipitation season has earlier cessation dates, while the
977 dry EoC WY, which is wetter than its historical counterpart, persists significantly longer into the
978 spring. As a consequence of warmer temperatures, all WYs show a substantial decrease in *SWE*.
979 The shift of precipitation from snowfall to rainfall, as well as the increase in the amount of
980 precipitation and the early start of precipitation lead to an overall increase in soil moisture and
981 more water available to meet the higher EoC *ET* demand. Importantly, this increase in *ET* is
982 heterogeneous across the watershed and highlights one of the main advantages of using an
983 integrated hydrologic model such as the one we employed in this study to assess the spatiotemporal

984 patterns of change. Our results show that the sensitivity to the changes in *ET* at EoC depends on
985 the subsurface geology and topographical gradients. More specifically:

- 986 • The geological and topographical complexities of the Sierra Nevada headwaters
987 lead to highly heterogeneous changes in *ET*. Changes in *ET* are higher in permeable
988 areas such as the plutonic rocks where water can be more easily extracted.
- 989 • *ET* changes in the Central Valley of the Cosumnes watershed are predominantly
990 uniform with the highest sensitivities in the vicinity of the Cosumnes River due to
991 the high availability of water.

992 Precipitation increases enough in the EoC to provide water for both increased *ET* and
993 increased surface water storage. Surface water storages also increase earlier in the WY and have
994 higher peak amounts. This earlier and larger increase is a direct consequence of an earlier start in
995 precipitation at EoC, a marked change in the precipitation phase, and an overall larger amount of
996 precipitation when compared with the historical WYs. However, our results also highlight that
997 during baseflow conditions surface water decreases, especially in lower-order streams, showing
998 that these areas are highly sensitive to the change in precipitation phase. Our simulations also show
999 that the seasonal variability of the EoC watershed behavior is also more dynamic. In general,
1000 decreases in seasonal water storages occurring between peak flow and baseflow conditions are
1001 more than 10% higher in the EoC compared to the historical conditions.

1002 EoC groundwater storages are also projected to increase earlier in the WY with peaks
1003 greater than those found historically. Yet these storages decrease significantly during baseflow
1004 conditions due to the higher *ET* at EoC and the absence of recharge from snowmelt. Contrary to
1005 the changes in surface water storages, groundwater storages show a larger decrease due to their
1006 dependence on the surface water from the Sierra Nevada. Our results also show that changes in

1007 subsurface pressure-heads are not uniform and are bi-directional throughout the Cosumnes
1008 watershed. Because the connectivity between the Central Valley aquifers and the Sierra Nevada
1009 headwaters (i.e., subsurface and surface flows from the headwater to the Central Valley aquifers)
1010 plays an important role in the hydrodynamics of this watershed, only areas with a strong connection
1011 with the headwaters, such as the foothills and the river channels, see an increase in subsurface
1012 pressure-heads at EoC. However, the subsurface pressure-heads decrease elsewhere in the Central
1013 Valley aquifers especially in baseflow conditions due to the high *ET* and the lack of snowmelt. In
1014 the river channels, this is due to the exchange between the subsurface and the surface whereas the
1015 foothills characterized by the consolidated sediments serve as “spillover.”

1016 Our results provide novel understandings about possible changes in the integrated
1017 hydrologic response to changes in EoC climate extremes. An important caveat is that our
1018 simulation was a single set of climate realizations and may not properly bound internal variability
1019 uncertainty like an ensemble of climate simulations could. However, beyond the widely agreed-
1020 upon changes of decreased snowpack and shifts in runoff timing in the literature, we show that in
1021 this simulation: 1) EoC precipitation increases even in the driest years; 2) despite increased
1022 temperature, and hence *ET*, both groundwater and surface water storage increase relative to
1023 historical conditions because of increased precipitation; and 3) there is a distinct spatial pattern,
1024 particularly in surface water storage, in which smaller-order streams see reduced flow while the
1025 larger order streams see increased flow. These changes will have strong implications on natural
1026 resource management.

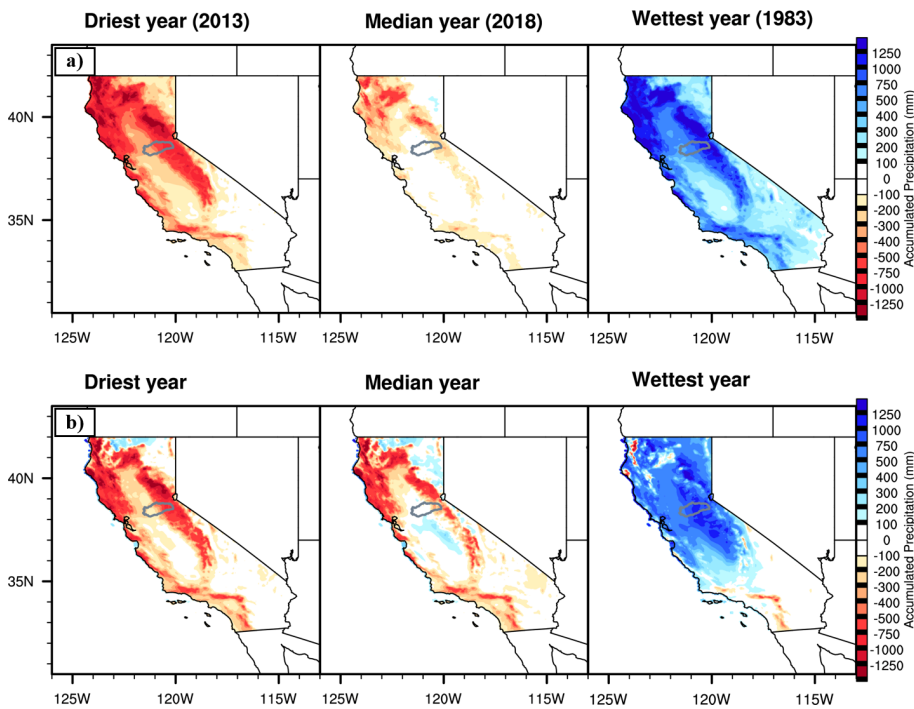
1027 In this study, land cover changes are assumed to not occur, however, changes in land cover
1028 are expected to occur in the future, either naturally or anthropogenically. Further vegetation
1029 physiology will also change in response to an increase in CO₂. Thus, future studies should

1030 investigate the impacts of these changes and how they may further alter the integrated hydrologic
1031 budgets. Additionally, future studies could also assess the effects of anthropogenic activities such
1032 as pumping and irrigation under a changing climate, other emissions scenarios, and/or the
1033 sequencing of variable end-member WYs and the interannual memory of the hydrologic system.
1034 Importantly, an understanding of this variability could be used to inform how water managers
1035 might prepare for more intense and/or intermittent extremes in the future. Future research could
1036 also use multiple emission scenarios to better assess the range in hydrodynamic responses
1037 dependent on the severity of climate change, especially those related to the magnitude and spatial
1038 location of the precipitation response since they are likely more uncertain and scenario-dependent
1039 than the trends at the watershed-scale.

1040 **Appendix A: Comparisons between VR-CESM and PRISM historical conditions**

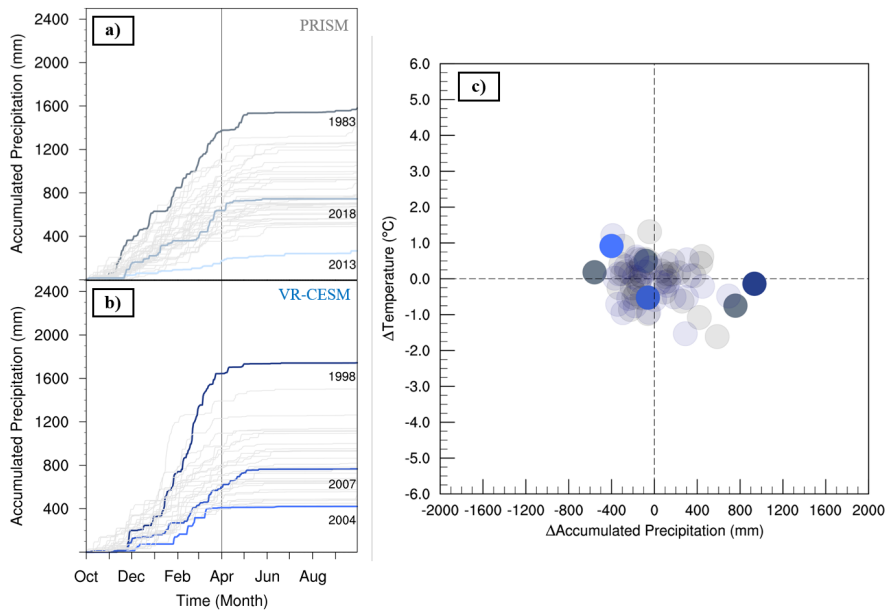
1041 Figure A1 highlights differences in dry, median, and wet WY accumulated precipitation
1042 relative to the 1981-2019 PRISM climatology. VR-CESM generally recreates the spatial pattern
1043 of anomalous dry and wet patterns across California for each WY type. This is shown via the
1044 common regions of minimum and maximum anomalies relative to the PRISM climatology.
1045 Notably, there are regions where VR-CESM anomalies are not consistent with PRISM. This is
1046 primarily shown in the wettest water year in portions of the Central Valley, western slopes of the
1047 Sierra Nevada, and southern California. This is likely correlated with resolution and the lack of
1048 orographic gradients (both valleys and peaks) in VR-CESM at 28km resolution. Mismatches in
1049 accumulated precipitation may also be due to representation of atmospheric rivers (ARs) in VR-
1050 CESM that were found to be generally larger, slightly more long-lived and make landfall more
1051 frequently over California (Rhoades et al., 2020b). Figure A2 shows Cosumnes watershed WY
1052 accumulated precipitation and surface temperature. WY accumulated precipitation is shown in
1053 Figure A 2a and 2b for PRISM and VR-CESM, respectively. All WY accumulated precipitation
1054 simulated by VR-CESM over 1985-2015 are within the range in PRISM, save for the wettest WY.
1055 This is shown more explicitly in quadrant space in Figure A2c where the range of annual bias in
1056 VR-CESM relative to the range of interannual variability in PRISM for accumulated precipitation
1057 and temperature is shown. VR-CESM generally simulates a wetter historical period over the
1058 Cosumnes (range of bias of 1330 mm) relative to PRISM (range of interannual variability of 1320
1059 mm). Basin-average minimum (421 mm) and maximum (1740 mm) WY accumulated
1060 precipitation are slightly larger than is found in PRISM. Of relevance to this study, PRISM has
1061 shown notable uncertainties in the Sierra Nevada. Lundquist et al., 2015 showed that an
1062 underrepresentation of the most extreme storm total precipitation in the Sierra Nevada can result

1063 in an upper-bound uncertainty of 20% in WY accumulated precipitation. Therefore, the wettest
1064 WY of VR-CESM is well within the 20% uncertainty range of PRISM's wettest WY (1580 ± 316
1065 mm). Further, differences in basin-average WY accumulated precipitation between VR-CESM
1066 and PRISM are non-significant using a t-test and assuming a p-value < 0.05 . The range of
1067 temperature bias in VR-CESM ($2.74\text{ }^{\circ}\text{C}$) relative to the range of PRISM interannual variability
1068 ($2.93\text{ }^{\circ}\text{C}$) was also within the temperature uncertainties discussed in Strachan and Daly, 2017.
1069 They showed that a general cool-bias in PRISM temperatures were found on the leeward side of the
1070 Sierra Nevada when compared with 16 out-of-sample in-situ observations across an elevation
1071 gradient of 1950 to 3100 meters with an overall mean bias of $-1.95\text{ }^{\circ}\text{C}$ (maximum temperature)
1072 and $-0.75\text{ }^{\circ}\text{C}$ (minimum temperature).



1073

1074 Figure A1: Differences in the driest, median, and wettest water year accumulated precipitation
 1075 over California in a) PRISM and b) VR-CESM relative to the 1981-2019 PRISM climatology.
 1076 The Cosumnes watershed boundary is outlined in gray.



1077
 1078 Figure A2: Cosumnes watershed accumulated precipitation totals in a) PRISM (gray; 1981-2019)
 1079 and b) VR-CESM (blue; 1985-2015) with dry, median, and wet years emboldened. c) shows
 1080 differences in PRISM (gray) and VR-CESM (blue) relative to the PRISM climatology (1981-2019)
 1081 in temperature and accumulated precipitation quadrant space. Dry, median, and wet water years
 1082 are emboldened.

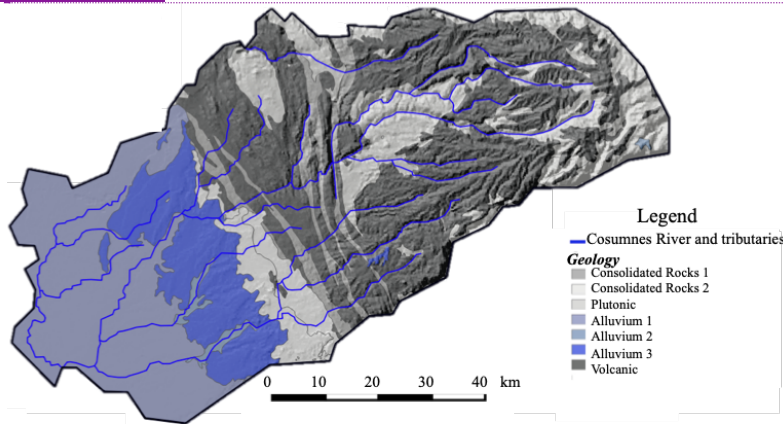
1083

1084

1085
1086

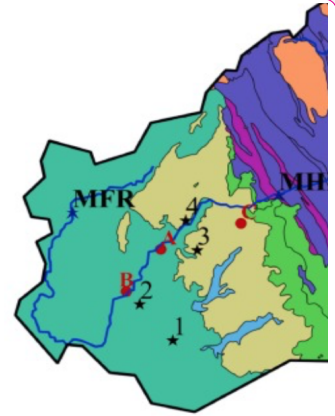
Appendix B: Integrated Hydrologic Model Parameterization

1. Input Variables



Formatted: Font: Bold

Formatted: Font color: Black



Deleted:

1087
1088
1089

Figure B1: Geological map of the Cosumnes watershed (source: USGS, Jennings et al., 1977)

Formatted: Font color: Black

Formatted: Font color: Black

Hydrodynamic properties based on the geology				
<u>Geological Formation</u>	<u>Porosity (-)</u>	<u>Specific Storage (m-1)</u>	<u>Van Genuchten α (m-1)</u>	<u>Van Genuchten n (-)</u>
<u>Bedrock (Consolidated, Plutonic and Volcanic Rocks)</u>	<u>0.02</u>	<u>10-6</u>	<u>3.0</u>	<u>3.0</u>
<u>Alluvial aquifers</u>	<u>0.2</u>	<u>10-4</u>	<u>3.0</u>	<u>3.0</u>

1090
1091
1092
1093

Table B1: Assigned values of hydrodynamic parameters (porosity, specific storage and Van Genuchten parameters). Values are based on literature review (Faunt et al., 2010; Faunt and Geological Survey (U.S.), 2009; Flint et al., 2013; Gilbert and Maxwell, 2017; Welch and Allen, 2014).

Formatted: Font color: Black

Formatted: Font color: Black

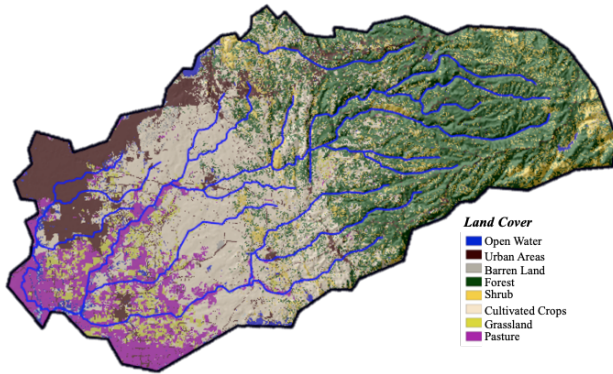
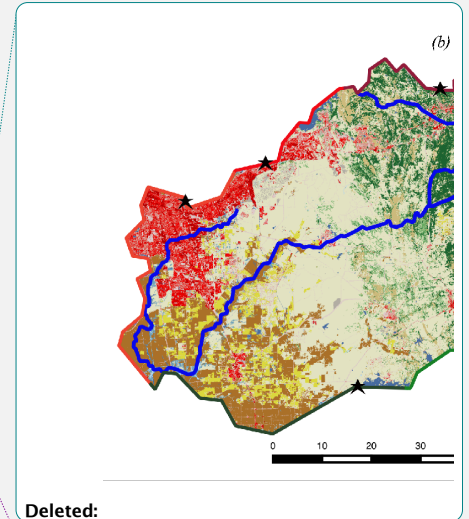


Figure B2: Cosumnes watershed characteristics: land use and land cover (source: Homer et al., 2015), and model boundaries.



Deleted:

Formatted: Font color: Black

Formatted: Font color: Black

Surface roughness based on land use			
Land Use	Manning Coefficient (h.m-1/3)		
Forest	5×10^{-2}		
Shrub land and agricultural area	5×10^{-3}		
Urban areas	5×10^{-5}		
Crop properties			
Crop Type and Reference	Height (m)	Maximum Leaf Area Index (-)	Minimum Leaf Area Index (-)
Alfalfa (Evetts et al., 2000; Orloff, 1995; Robison et al., 1969)	0.6	6.0	2.0
Pasture (Buermann et al., 2002; King et al., 1986; Rahman and Lamb, 2017)	0.12	6.0	1.0
Vineyards (Johnson and Pierce, 2004; Vanino et al., 2015)	0.9	3.0	0.6

Table B2: Manning coefficients and crop properties

Formatted: Font color: Black

Formatted: Font color: Black

Boundary conditions	Value
Mokelumne and American river	Weekly-varying Dirichlet boundary conditions. These values are based on the measured river stages.
Sierra Nevada limit	No flow Neumann boundary condition
Bottom of the model	No flow Neumann boundary condition

Table B3: boundary conditions

Formatted: Font color: Black

Formatted: Font color: Black

1105
1106

2. Numerical model set-up

Domain size	~7000 km ²																											
Spatial discretization	200 m horizontal from 0.1 m to 30 m in the vertical direction <table border="1" style="margin-left: 20px;"> <tr> <th colspan="9">Vertical Resolution</th> </tr> <tr> <th>Layer</th> <th>1</th> <th>2</th> <th>3</th> <th>4</th> <th>5</th> <th>6</th> <th>7</th> <th>8</th> </tr> <tr> <th>$\Delta z(m)$</th> <td>0.1</td> <td>0.3</td> <td>0.6</td> <td>1.0</td> <td>8.0</td> <td>15.0</td> <td>25.0</td> <td>30.0</td> </tr> </table>	Vertical Resolution									Layer	1	2	3	4	5	6	7	8	$\Delta z(m)$	0.1	0.3	0.6	1.0	8.0	15.0	25.0	30.0
Vertical Resolution																												
Layer	1	2	3	4	5	6	7	8																				
$\Delta z(m)$	0.1	0.3	0.6	1.0	8.0	15.0	25.0	30.0																				
Simulation time	Model validation (from water year 2012 to water year 2017), then future water years																											
Temporal discretization	hourly																											

Table B4: Numerical model discretization

Formatted: Font color: Black

Formatted: Font: Bold

Formatted: List Paragraph, Outline numbered + Level: 1 + Numbering Style: 1, 2, 3, ... + Start at: 1 + Alignment: Left + Aligned at: 0.25" + Indent at: 0.5"

1107
1108
1109
1110

3. Output variables

Selected output variables	Temporal scale	Spatial scale
Snow Water Equivalent	Yearly, monthly, and hourly	Domain-average and point scale
Evapotranspiration	Yearly, monthly, and hourly	Domain-average and point scale
Soil Moisture	Yearly, monthly, and hourly	Domain-average and point scale
River Stages (also surface water storages)	Yearly, monthly, and hourly	Domain-average and point scale
Groundwater levels variations (also subsurface storages)	Yearly, monthly, and hourly	Domain-average and point scale

Table B5: Selected output variables

Formatted: Font color: Black

Formatted: Font color: Black

Formatted: Font color: Black

Formatted: Font: Bold

Formatted: List Paragraph, Outline numbered + Level: 1 + Numbering Style: 1, 2, 3, ... + Start at: 1 + Alignment: Left + Aligned at: 0.25" + Indent at: 0.5"

1111
1112

Formatted: Font color: Black

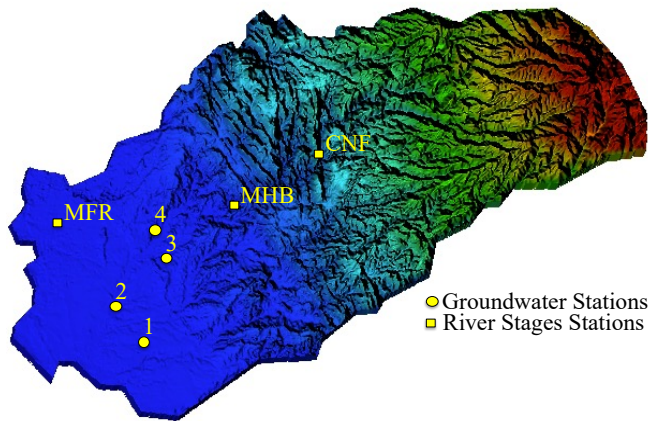
Formatted: Font color: Black

1113

1114

1115 **Appendix C: Integrated Hydrologic Model Validation**

1116 We compared temporal variations of streamflow at 3 stations located in the Sierra
1117 (uplands), the intersection between the Sierra and the Central Valley, and the outskirts of
1118 Sacramento (see Figure C1). Four wells in the watershed (see Figure C1) have reasonable, publicly
1119 available records of groundwater levels and were used to check the ability of the model to
1120 reproduce water table depth variations.



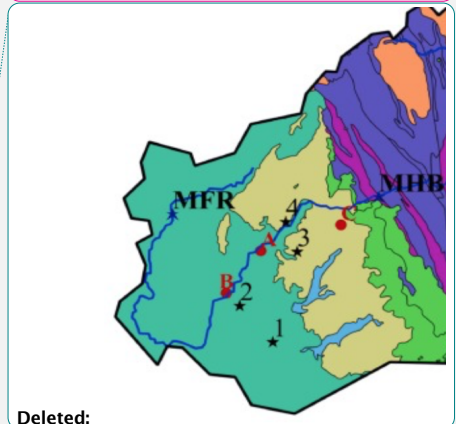
1121
1122 Figure C1: The locations of the 3 streamflow gauges (CNF, MHB, and MFR) and 4
1123 groundwater wells (stars).

1124
1125 Figure C2a depicts the comparisons between simulated and measured river stages at the 3
1126 stations indicated in figure C1. Absolute errors (L1) in m and relative errors (L2) are shown in
1127 Table C1. Differences between simulated and measured streamflow vary between 0.4 and 0.8 m
1128 (Table C1) indicating that the model is able to reproduce the river dynamics.

1129 Absolute differences given by:

- Formatted: Font: Bold
- Formatted: Justified, Indent: First line: 0.5", Line spacing: Double
- Formatted: Font color: Auto
- Formatted: Font: Bold
- Formatted: Font: Not Italic
- Deleted: publicly-available
- Formatted: Font: Not Italic
- Formatted: Font: Not Italic
- Formatted: Font: Not Italic

Formatted: Indent: First line: 0.5", Line spacing: Double



- Deleted:
- Formatted: Font color: Auto
- Formatted: Justified, Indent: First line: 0.5", Line spacing: Double
- Formatted: Font color: Auto
- Formatted: Space After: 0 pt

1132 $L_{1i,j} = |X_{mes_{i,j}} - X_{sim_{i,j}}|$ (C1)

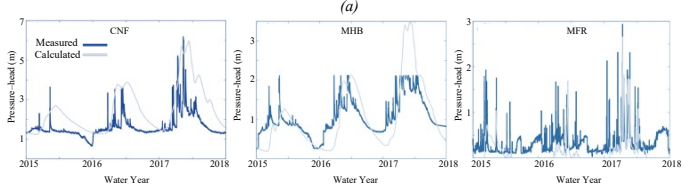
1133 Where $L_{1i,j}$ is the absolute difference associated with cell i and time j . $X_{mes_{i,j}}$ is the
 1134 measured (or remotely sensed) data, and $X_{sim_{i,j}}$ the simulated value.

1135 Relative differences $L_{2i,j}$ are given by:

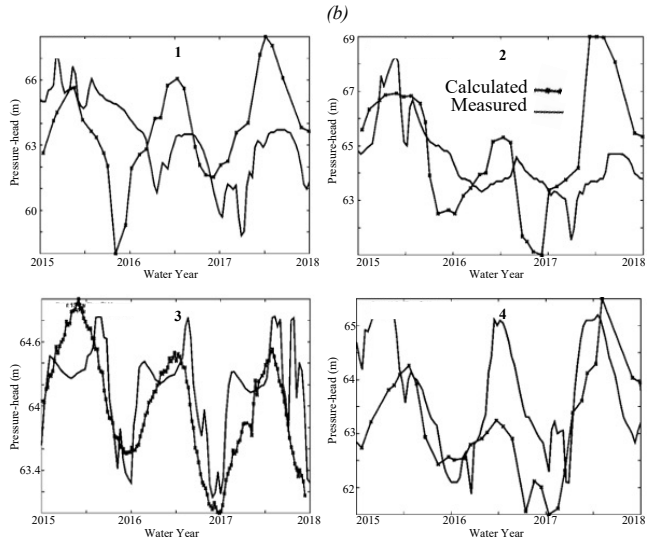
1136 $L_{2i,j} = \frac{|X_{mes_{i,j}} - X_{sim_{i,j}}|}{X_{mes_{i,j}}}$ (C2)

Formatted: Centered

1137 (a)



1138 (b)



1139 Figure C2: Comparisons between measured and calculated (a) river stages (i.e., pressure-
 1140 heads simulated by ParFlow-CLM) and (b) subsurface pressure-head. The location of the selected
 1141 points is indicated in Figure C1.

1142

<u>Measurements</u>	<u>L1 (m)</u>	<u>L2 (-)</u>
<u>River Stages (CNF)</u>	<u>0.8</u>	<u>0.5</u>
<u>River Stages (MHB)</u>	<u>0.4</u>	<u>0.36</u>
<u>River Stages (MFR)</u>	<u>0.57</u>	<u>1.06</u>
<u>Groundwater Levels (Well 1)</u>	<u>3.73</u>	<u>0.05</u>
<u>Groundwater Levels (Well 2)</u>	<u>1.63</u>	<u>0.02</u>
<u>Groundwater Levels (Well 3)</u>	<u>0.476</u>	<u>0.0077</u>
<u>Groundwater Levels (Well 4)</u>	<u>1.08</u>	<u>0.016</u>

1143 Table C1: Differences between measured and calculated surface and groundwater levels. L1 is the
 1144 absolute error and R2 the relative error.

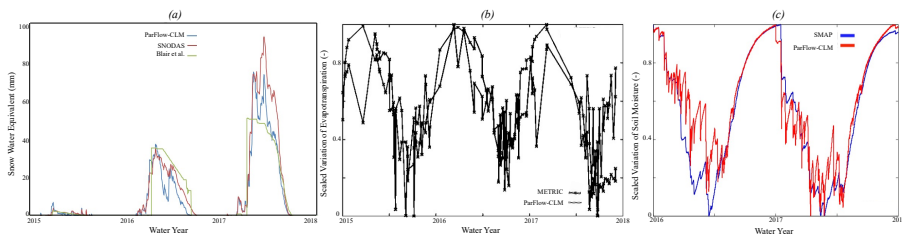
Formatted: Indent: First line: 0"

1145

1146 Comparisons between simulated and calculated groundwater levels (here referred to as the
 1147 pressure-heads at the bottom of the domain) shown in Figure C2b indicate that the model has
 1148 reasonable agreements with measurements. As shown in table C1, the error varies between 0.47 to
 1149 3.73 m depending on the station. Mismatches between simulated and observed groundwater levels
 1150 at wells 1 and 2 are likely due to an inaccurate estimation of pumping in these areas. The temporal
 1151 variations of the groundwater levels show an impact of withdrawals but because these withdrawals
 1152 are hard to estimate the model isn't correctly reproducing these trends.

1153

1154 ParFlow-CLM also solves the key land surface processes governing the transfer of water
 1155 and energy at the land-atmosphere-soil interface: evapotranspiration, snow dynamics, and soil
 1156 moisture. In Maina et al., (2020a), rigorous comparisons between the ParFlow-CLM simulated
 1157 land surface processes and remotely sensed estimates of these variables were conducted (Figure
 1158 C3). Table C2 shows the correlation coefficient between ParFlow-CLM results and the various
 1159 datasets compared.



1160
 1161 Figure C3: (a) Comparisons between domain-averaged total snow water equivalent obtained with
 1162 ParFlow-CLM, SNODAS and Bair et al., reconstruction, (b) Comparisons between actual
 1163 evapotranspiration obtained with ParFlow-CLM and METRIC (c) Relative variation of soil
 1164 moisture obtained with ParFlow-CLM and SMAP. Note that the x-axis of (c) is shorter because of
 1165 the availability of SMAP data

Formatted: Indent: First line: 0"

<u>Satellites based products</u>	<u>L1 (m)</u>	<u>L2 (-)</u>	<u>Pearson Correlation Coefficient</u>
<u>SWE SNODAS (mm)</u>	<u>3.09</u>	<u>3.77</u>	<u>0.97</u>
<u>SWE Bair et al., (mm)</u>	<u>3.80</u>	<u>2.69</u>	<u>0.84</u>
<u>Soil Moisture SMAP (-)</u>	<u>0.217</u>	<u>3.07</u>	<u>0.94</u>
<u>ET METRIC (mm/s)</u>	<u>0.067</u>	<u>1.40</u>	<u>0.6</u>

1167 [Table C2: differences between measured and remotely sensed evapotranspiration \(METRIC\), soil](#)
1168 [moisture \(SMAP\), and snow water equivalent \(SNODAS and Bair et al., 2016\)](#)

1170 Data availability

1171 Data supporting the findings of this study can be found here:
1172 <https://portal.nersc.gov/archive/home/a/arhoades/Shared/www/Hyperion/>

1173 Author contribution

1174 The authors contribute equally to this work.

1175 Competing interests

1176 The authors declare that they have no conflict of interest.

1177 Acknowledgements

1178 Fadjri Zaouna Maina and Erica Siirila-Woodburn were supported by LDRD funding from Berkeley
1179 Lab, provided by the Director, Office of Science, of the U.S. Department of Energy under Contract
1180 No. DE-AC02-05CH11231.

1181 Author Alan M. Rhoades was funded by the Department of Energy, Office of Science Office of
1182 Biological and Environmental Research program under Award Number DE-SC0016605 "A
1183 framework for improving analysis and modeling of Earth system and intersectoral dynamics at
1184 regional scales" and Award Number DE-AC02-05CH11231 "The Calibrated and Systematic
1185 Characterization, Attribution, and Detection of Extremes - Science Focus Area".

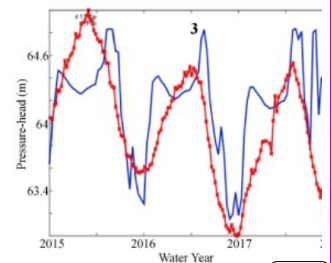
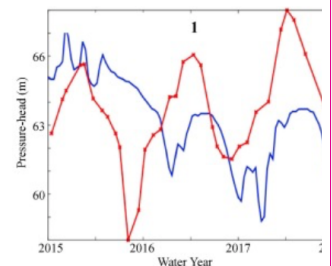
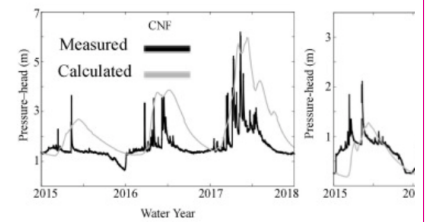
1186 This research used computing resources from the National Energy Research Scientific
1187 Computing Center, a DOE Office of Science User Facility supported by the [http://](http://dx.doi.org/10.13039/100006132)
1188 dx.doi.org/10.13039/100006132 of the U.S. Department of Energy under Contract No. DE-
1189 AC02-05CH11231.

Formatted: Indent: First line: 0"

Deleted: Absolute differences given by:

(C1)
Where Δ is the absolute difference associated with cell i and time j , M is the measured (or remotely sensed) data, and S the simulated value.
Relative differences are given by:

(C2)



1217
1218
1219

References

1220 [Abbott, M. B., J. C. Bathurst, J. A. Cunge, P. E. Oconnell, and J. Rasmussen \(1986\), An](#)
1221 [introduction to the european hydrological system: Sys- teme hydrologique Europeen. She](#)
1222 [.2. Structure of a physically-based, distributed modeling system, J. Hydrol., 87\(1-2\), 61-](#)
1223 [77.](#)

Formatted: Font color: Text 1

1224 Allan, R.P., Barlow, M., Byrne, M.P., Cherchi, A., Douville, H., Fowler, H.J., Gan, T.Y.,
1225 Pendergrass, A.G., Rosenfeld, D., Swann, A.L.S., Wilcox, L.J. and Zolina, O. (2020),
1226 Advances in understanding large-scale responses of the water cycle to climate change.
1227 Ann. N.Y. Acad. Sci., 1472: 49-75. <https://doi.org/10.1111/nyas.14337>

1228 [Allen R. G., Masahiro T., Ricardo T. \(2007\)Satellite-based energy balance for mapping](#)
1229 [evapotranspiration with internalized calibration \(METRIC\)—model J. Irrig. Drain.](#)
1230 [Eng., 133, pp. 380-394, 10.1061/\(ASCE\)0733-9437\(2007\) 133:4\(380\).](#)

Formatted: Font color: Text 1

1231 Alo, C. A., & Wang, G. (2008). Hydrological impact of the potential future vegetation response to
1232 climate changes projected by 8 GCMs. *Journal of Geophysical Research: Biogeosciences*,
1233 113(G3). <https://doi.org/10.1029/2007JG000598>

1234 [Bair E.H., Rittger K., Davis R.E., Painter T.H., Dozier J. \(2016\) Validating reconstruction of snow](#)
1235 [water equivalent in California's Sierra Nevada using measurements from the NASA](#)
1236 [Airborne Snow Observatory Water Resour. Res., 52 , pp. 8437-](#)
1237 [8460, 10.1002/2016WR018704.](#)

Formatted: Font color: Text 1

1238 Bales, R. C., Molotch, N. P., Painter, T. H., Dettinger, M. D., Rice, R., & Dozier, J. (2006).
1239 Mountain hydrology of the western United States. *Water Resources Research*, 42(8).
1240 <https://doi.org/10.1029/2005WR004387>

1241 Barnett, T. P., Adam, J. C., & Lettenmaier, D. P. (2005). Potential impacts of a warming climate
1242 on water availability in snow-dominated regions. *Nature*, *438*(7066), 303–309.
1243 <https://doi.org/10.1038/nature04141>

1244 Berghuijs, W. R., Woods, R. A., & Hrachowitz, M. (2014). A precipitation shift from snow
1245 towards rain leads to a decrease in streamflow. *Nature Climate Change*, *4*(7), 583–586.
1246 <https://doi.org/10.1038/nclimate2246>

1247 [Bixio, A. C., G. Gambolati, C. Paniconi, M. Putti, V. M. Shestopalov, V. N. Bubljas, A. S.](#)
1248 [Bohuslavsky, N. B. Kastel'tseva, and Y. F. Rudenko \(2002\). Modeling groundwater-](#)
1249 [surface water interactions including effects of morphogenetic depressions in the Chernobyl](#)
1250 [exclusion zone. *Environ. Geol.*, *42*\(2-3\) 162-177.](#)

1251 Cayan, D. R., Maurer, E. P., Dettinger, M. D., Tyree, M., & Hayhoe, K. (2008). Climate change
1252 scenarios for the California region. *Climatic Change*, *87*(1), 21–42.
1253 <https://doi.org/10.1007/s10584-007-9377-6>

1254 Christensen, L., Tague, C. L., & Baron, J. S. (2008). Spatial patterns of simulated transpiration
1255 response to climate variability in a snow dominated mountain ecosystem. *Hydrological*
1256 *Processes*, *22*(18), 3576–3588. <https://doi.org/10.1002/hyp.6961>

1257 Collins, W. D., Bitz, C. M., Blackmon, M. L., Bonan, G. B., Bretherton, C. S., Carton, J. A., et al.
1258 (2006). The Community Climate System Model Version 3 (CCSM3). *Journal of Climate*,
1259 *19*(11), 2122–2143. <https://doi.org/10.1175/JCLI3761.1>

1260 Condon, L. E., Maxwell, R. M., & Gangopadhyay, S. (2013). The impact of subsurface
1261 conceptualization on land energy fluxes. *Advances in Water Resources*, *60*, 188–203.
1262 <https://doi.org/10.1016/j.advwatres.2013.08.001>

Formatted: Font color: Text 1

1263 Condon, L.E., Atchley, A.L., Maxwell, R.M., (2020). Evapotranspiration depletes groundwater
1264 under warming over the contiguous United States. *Nature Communications* 11, 873.
1265 <https://doi.org/10.1038/s41467-020-14688-0>

1266 Cook, E. R., Woodhouse, C. A., Eakin, C. M., Meko, D. M., & Stahle, D. W. (2004). Long-Term
1267 Aridity Changes in the Western United States. *Science*, 306(5698), 1015–1018.
1268 <https://doi.org/10.1126/science.1102586>

1269 [Coon, E. T., J. D. Moulton, and S. L. Painter \(2016\), Managing complexity in simulations of land](#)
1270 [surface and near-surface processes, *Environ. Modell Software*, 78, 134-149,](#)

1271 Cosgrove, B. A., Lohmann, D., Mitchell, K. E., Houser, P. R., Wood, E. F., Schaake, J. C., et al.
1272 (2003). Real-time and retrospective forcing in the North American Land Data Assimilation
1273 System (NLDAS) project. *Journal of Geophysical Research: Atmospheres*, 108(D22).
1274 <https://doi.org/10.1029/2002JD003118>

1275 Cristea, N. C., Lundquist, J. D., Loheide, S. P., Lowry, C. S., & Moore, C. E. (2014). Modelling
1276 how vegetation cover affects climate change impacts on streamflow timing and magnitude
1277 in the snowmelt-dominated upper Tuolumne Basin, Sierra Nevada. *Hydrological*
1278 *Processes*, 28(12), 3896–3918. <https://doi.org/10.1002/hyp.9909>

1279 Daly, C., Halbleib, M., Smith, J. I., Gibson, W. P., Doggett, M. K., Taylor, G. H., et al. (2008).
1280 Physiographically sensitive mapping of climatological temperature and precipitation across the
1281 conterminous United States. *International Journal of Climatology*, 28(15), 2031–2064.
1282 <https://doi.org/10.1002/joc.1688>.

1283 Dettinger, M. (2011). Climate Change, Atmospheric Rivers, and Floods in California – A
1284 Multimodel Analysis of Storm Frequency and Magnitude Changes1. *JAWRA Journal of*

Formatted: Font color: Text 1

1285 *the American Water Resources Association*, 47(3), 514–523.
1286 <https://doi.org/10.1111/j.1752-1688.2011.00546.x>

1287 Dettinger, M., & Anderson, M. L. (2015). Storage in California’s reservoirs and snowpack in this
1288 time of drought. *San Francisco Estuary and Watershed Science*, 13(2).
1289 <https://doi.org/10.15447/sfews.2015v13iss2art1>

1290 Dettinger, M., Redmond, K., & Cayan, D. (2004). Winter Orographic Precipitation Ratios in the
1291 Sierra Nevada—Large-Scale Atmospheric Circulations and Hydrologic Consequences.
1292 *Journal of Hydrometeorology*, 5(6), 1102–1116. <https://doi.org/10.1175/JHM-390.1>

1293 Dettinger, M. D. (2013). Atmospheric Rivers as Drought Busters on the U.S. West Coast. *Journal*
1294 *of Hydrometeorology*, 14(6), 1721–1732. <https://doi.org/10.1175/JHM-D-13-02.1>

1295 Di Liberto, T. (2017, October). Very wet 2017 WY ends in California. *NOAA Climate.Gov*.
1296 Retrieved from [https://www.climate.gov/news-features/featured-images/very-wet-2017-](https://www.climate.gov/news-features/featured-images/very-wet-2017-water-year-ends-california)
1297 [water-year-ends-california](https://www.climate.gov/news-features/featured-images/very-wet-2017-water-year-ends-california)

1298 Dierauer, J. R., Whitfield, P. H., & Allen, D. M. (2018). Climate Controls on Runoff and Low
1299 Flows in Mountain Catchments of Western North America. *Water Resources Research*,
1300 54(10), 7495–7510. <https://doi.org/10.1029/2018WR023087>

1301 Faunt, C.C., Belitz, K., Hanson, R.T., 2010. Development of a three-dimensional model of
1302 sedimentary texture in valley-fill deposits of Central Valley, California, USA.
1303 *Hydrogeology Journal* 18, 625–649. <https://doi.org/10.1007/s10040-009-0539-7>

1304 Faunt, C.C., Geological Survey (U.S.) (Eds.), 2009. Groundwater availability of the Central Valley
1305 Aquifer, California, U.S. Geological Survey professional paper. U.S. Geological Survey,
1306 Reston, Va.

1307 Ficklin, D. L., Luo, Y., & Zhang, M. (2013). Climate change sensitivity assessment of streamflow
1308 and agricultural pollutant transport in California's Central Valley using Latin hypercube
1309 sampling. *Hydrological Processes*, 27(18), 2666–2675. <https://doi.org/10.1002/hyp.9386>

1310 Foster, L. M., Williams, K. H., & Maxwell, R. M. (2020). Resolution matters when modeling
1311 climate change in headwaters of the Colorado River. *Environmental Research Letters*.
1312 <https://doi.org/10.1088/1748-9326/aba77f>

1313 Gates WL (1992) AMIP: the atmospheric model intercomparison project. *Bull Am Meteorol Soc*
1314 73(12):1962–1970. doi:10.1175/1520-0477(1992)073<1962:ATAMIP>2.0.CO;2

1315 Geologic Map of California, 2015. Geologic Map of California [WWW Document]. Geologic Map
1316 of California. URL <https://maps.conservation.ca.gov/cgs/gmc/> (accessed 10.17.18).

1317 Gent, P. R., Danabasoglu, G., Donner, L. J., Holland, M. M., Hunke, E. C., Jayne, S. R., et al.
1318 (2011). The Community Climate System Model Version 4. *Journal of Climate*, 24(19),
1319 4973–4991. <https://doi.org/10.1175/2011JCLI4083.1>

1320 Gershunov, A., Shulgina, T., Clemesha, R.E.S. et al. (2019). Precipitation regime change in
1321 Western North America: The role of Atmospheric Rivers. *Sci Rep* 9, 9944.
1322 <https://doi.org/10.1038/s41598-019-46169-w>

1323 Gettelman, A., and Morrison, H. (2015). Advanced Two-Moment Bulk Microphysics for Global
1324 Models. Part I: Off-Line Tests and Comparison with Other Schemes. *Journal of Climate*
1325 28, 3, 1268-1287. <https://doi.org/10.1175/JCLI-D-14-00102.1>

1326 Gilbert, J.M., Maxwell, R.M., 2017. Examining regional groundwater - surface water dynamics
1327 using an integrated hydrologic model of the San Joaquin River basin. *Hydrology and Earth*
1328 *System Sciences* 21, 923–947. <https://doi.org/10.5194/hess-21-923-2017>

- 1329 Gleick, P. H. (1987). The development and testing of a water balance model for climate impact
1330 assessment: Modeling the Sacramento Basin. *Water Resources Research*, 23(6), 1049–
1331 1061. <https://doi.org/10.1029/WR023i006p01049>
- 1332 Godsey, S. E., Kirchner, J. W., & Tague, C. L. (2014). Effects of changes in winter snowpacks on
1333 summer low flows: case studies in the Sierra Nevada, California, USA. *Hydrological*
1334 *Processes*, 28(19), 5048–5064. <https://doi.org/10.1002/hyp.9943>
- 1335 Griffin, D., & Anchukaitis, K. J. (2014). How unusual is the 2012–2014 California drought?
1336 *Geophysical Research Letters*, 41(24), 9017–9023.
1337 <https://doi.org/10.1002/2014GL062433>
- 1338 Haarsma, R. J., Roberts, M. J., Vidale, P. L., Senior, C. A., Bellucci, A., Bao, Q., Chang, P., Corti,
1339 S., Fučkar, N. S., Guemas, V., von Hardenberg, J., Hazeleger, W., Kodama, C., Koenig,
1340 T., Leung, L. R., Lu, J., Luo, J.-J., Mao, J., Mizielinski, M. S., Mizuta, R., Nobre, P., Satoh,
1341 M., Scoccimarro, E., Semmler, T., Small, J., and von Storch, J.-S. (2016). High Resolution
1342 Model Intercomparison Project (HighResMIP v1.0) for CMIP6, *Geosci. Model Dev.*, 9,
1343 4185–4208, <https://doi.org/10.5194/gmd-9-4185-2016>.
- 1344 [Harbaugh AW \(2005\) MODFLOW-2005, The U.S. Geological Survey modular ground-water
1345 model: the ground-water flow process. US Geol Surv Tech Methods 6-
1346 A16. http://pubs.usgs.gov/tm/2005/tm6A16/.](http://pubs.usgs.gov/tm/2005/tm6A16/)
- 1347 Harpold, A. A., & Molotch, N. P. (2015). Sensitivity of soil water availability to changing
1348 snowmelt timing in the western U.S. *Geophysical Research Letters*, 42(19), 8011–8020.
1349 <https://doi.org/10.1002/2015GL065855>
- 1350 Hayhoe, K., Cayan, D., Field, C. B., Frumhoff, P. C., Maurer, E. P., Miller, N. L., et al. (2004).
1351 Emissions pathways, climate change, and impacts on California. *Proceedings of the*

Formatted: Font color: Text 1

1352 *National Academy of Sciences*, 101(34), 12422–12427.
1353 <https://doi.org/10.1073/pnas.0404500101>

1354 He, M., Anderson, M., Schwarz, A., Das, T., Lynn, E., Anderson, J., et al. (2019). Potential
1355 Changes in Runoff of California’s Major Water Supply Watersheds in the 21st Century.
1356 *Water*, 11(8), 1651. <https://doi.org/10.3390/w11081651>

1357 Herrington, A. R., P. H. Lauritzen, M. A. Taylor, S. Goldhaber, B. E. Eaton, J. T. Bacmeister, K.
1358 A. Reed, and P. A. Ullrich (2019). Physics–Dynamics Coupling with Element-Based High-
1359 Order Galerkin Methods: Quasi-Equal-Area Physics Grid. *Mon. Wea. Rev.*, 147, 69–84,
1360 <https://doi.org/10.1175/MWR-D-18-0136.1>.

1361 Homer, C., Dewitz, J., Yang, L., Jin, S., Danielson, P., Xian, G., et al. (2015). Completion of the
1362 2011 National Land Cover Database for the conterminous United States—representing a
1363 decade of land cover change information. *Photogrammetric Engineering & Remote*
1364 *Sensing*, 81(5), 345–354.

1365 Huang, X., Rhoades, A. M., Ullrich, P. A., & Zarzycki, C. M. (2016). An evaluation of the
1366 variable-resolution CESM for modeling California’s climate. *Journal of Advances in*
1367 *Modeling Earth Systems*, 8(1), 345–369. <https://doi.org/10.1002/2015MS000559>

1368 Huang, X., Stevenson, S., & Hall, A. D. (2020). Future warming and intensification of
1369 precipitation extremes: A “double whammy” leading to increasing flood risk in California.
1370 *Geophysical Research Letters*, 47, e2020GL088679.
1371 <https://doi.org/10.1029/2020GL088679>

1372 Hurrell, J. W., Holland, M. M., Gent, P. R., Ghan, S., Kay, J. E., Kushner, P. J., et al. (2013). The
1373 Community Earth System Model: A Framework for Collaborative Research. *Bulletin of*

1374 *the American Meteorological Society*, 94(9), 1339–1360. <https://doi.org/10.1175/BAMS->
1375 D-12-00121.1

1376 Jones, P. W., (1999). First- and Second-Order Conservative Remapping Schemes for Grids in
1377 Spherical Coordinates. *Mon. Wea. Rev.*, 127, 2204–2210, <https://doi.org/10.1175/1520->
1378 [0493\(1999\)127<2204:FASOCR>2.0.CO;2](https://doi.org/10.1175/1520-0493(1999)127<2204:FASOCR>2.0.CO;2).

1379 IGBP, 2018. Global plant database published - IGBP [WWW Document]. URL
1380 <http://www.igbp.net/news/news/globalplantdatabasepublished.5.1b8ae20512db692f>
1381 [2a6800014762.html](http://www.igbp.net/news/news/globalplantdatabasepublished.5.1b8ae20512db692f2a6800014762.html) (accessed 10.17.18).

1382 Jennings, C. W., Strand, R. G., & Rogers, T. H. (1977). Geologic map of California. Sacramento,
1383 Calif.: Division of Mines and Geology.

1384 Kampenhout, L. van, Rhoades, A. M., Herrington, A. R., Zarzycki, C. M., Lenaerts, J. T. M.,
1385 Sacks, W. J., & Broeke, M. R. van den. (2019). Regional grid refinement in an Earth system
1386 model: impacts on the simulated Greenland surface mass balance. *The Cryosphere*, 13(6),
1387 1547–1564. <https://doi.org/10.5194/tc-13-1547-2019>

1388 Kollet, S. J., & Maxwell, R. M. (2006). Integrated surface–groundwater flow modeling: A free-
1389 surface overland flow boundary condition in a parallel groundwater flow model. *Advances*
1390 *in Water Resources*, 29(7), 945–958. <https://doi.org/10.1016/j.advwatres.2005.08.006>

1391 Lemordant, L., Gentine, P., Swann, A. S., Cook, B. I., & Scheff, J. (2018). Critical impact of
1392 vegetation physiology on the continental hydrologic cycle in response to increasing CO₂.
1393 *Proceedings of the National Academy of Sciences*, 115(16), 4093–4098.
1394 <https://doi.org/10.1073/pnas.1720712115>

1395 [Liang, X., D. P. Lettenmaier, E. F. Wood, and S. J. Burges \(1994\), A simple hydrologically based](#)
1396 [model of land surface water and energy fluxes for general circulation models, *J. Geophys.*](#)
1397 [Res., 99\(D7\), 14415–14428, doi:10.1029/94JD00483,](#)

1398 Lundquist, J. D., Hughes, M., Henn, B., Gutmann, E. D., Livneh, B., Dozier, J., & Neiman, P.
1399 (2015). High-Elevation Precipitation Patterns: Using Snow Measurements to Assess Daily
1400 Gridded Datasets across the Sierra Nevada, California, *Journal of Hydrometeorology*,
1401 16(4), 1773-1792. doi: [https://journals.ametsoc.org/view/journals/hydr/16/4/jhm-d-15-](https://journals.ametsoc.org/view/journals/hydr/16/4/jhm-d-15-0019_1.xml)
1402 [0019_1.xml](https://journals.ametsoc.org/view/journals/hydr/16/4/jhm-d-15-0019_1.xml)

1403 Maina, Fadji Z., Siirila-Woodburn, E. R., Newcomer, M., Xu, Z., & Steefel, C. (2020a).
1404 Determining the impact of a severe dry to wet transition on watershed hydrodynamics in
1405 California, USA with an integrated hydrologic model. *Journal of Hydrology*, 580, 124358.
1406 <https://doi.org/10.1016/j.jhydrol.2019.124358>

1407 Maina, F. Z., Siirila-Woodburn, E. R., & Vahmani, P. (2020b). Sensitivity of meteorological-
1408 forcing resolution on hydrologic variables. *Hydrology and Earth System Sciences*, 24(7),
1409 3451–3474. <https://doi.org/10.5194/hess-24-3451-2020>

1410 Maina, Fadji Zaoua, & Siirila-Woodburn, E. R. (2020c). Watersheds dynamics following
1411 wildfires: Nonlinear feedbacks and implications on hydrologic responses. *Hydrological*
1412 *Processes*, 34(1), 33–50. <https://doi.org/10.1002/hyp.13568>

1413 Mallakpour, I., Sadegh, M., AghaKouchak, A., 2018. A new normal for streamflow in California
1414 in a warming climate: Wetter wet seasons and drier dry seasons. *Journal of Hydrology* 567,
1415 203–211. <https://doi.org/10.1016/j.jhydrol.2018.10.023>

Formatted: Font color: Text 1

1416 Maurer, E. P. (2007). Uncertainty in hydrologic impacts of climate change in the Sierra Nevada,
1417 California, under two emissions scenarios. *Climatic Change*, 82(3), 309–325.
1418 <https://doi.org/10.1007/s10584-006-9180-9>

1419 Maurer, E. P., & Duffy, P. B. (2005). Uncertainty in projections of streamflow changes due to
1420 climate change in California. *Geophysical Research Letters*, 32(3).
1421 <https://doi.org/10.1029/2004GL021462>

1422 Maxwell, R. M. (2013). A terrain-following grid transform and preconditioner for parallel, large-
1423 scale, integrated hydrologic modeling. *Advances in Water Resources*, 53, 109–117.
1424 <https://doi.org/10.1016/j.advwatres.2012.10.001>

1425 Maxwell, R. M., & Condon, L. E. (2016). Connections between groundwater flow and
1426 transpiration partitioning. *Science*, 353(6297), 377–380.
1427 <https://doi.org/10.1126/science.aaf7891>

1428 Maxwell, R. M., & Miller, N. L. (2005). Development of a Coupled Land Surface and
1429 Groundwater Model. *Journal of Hydrometeorology*, 6(3), 233–247.
1430 <https://doi.org/10.1175/JHM422.1>

1431 Mayer, T. D., & Naman, S. W. (2011). Streamflow Response to Climate as Influenced by Geology
1432 and Elevation1. *JAWRA Journal of the American Water Resources Association*, 47(4),
1433 724–738. <https://doi.org/10.1111/j.1752-1688.2011.00537.x>Boryan, C., Yang, Z.,
1434 Mueller, R., Craig, M., 2011. Monitoring US agriculture: the US Department of
1435 Agriculture, National Agricultural Statistics Service, Cropland Data Layer Program.
1436 Geocarto International 26, 341–358. <https://doi.org/10.1080/10106049.2011.562309>

1437 Mallakpour, I., Sadegh, M., AghaKouchak, A., 2018. A new normal for streamflow in California
1438 in a warming climate: Wetter wet seasons and drier dry seasons. *Journal of Hydrology* 567,
1439 203–211. <https://doi.org/10.1016/j.jhydrol.2018.10.023>

1440 Maxwell, R.M., 2013. A terrain-following grid transform and preconditioner for parallel, large-
1441 scale, integrated hydrologic modeling. *Advances in Water Resources* 53, 109–117.
1442 <https://doi.org/10.1016/j.advwatres.2012.10.001>

1443 McEvoy, D.J., Pierce, D.W., Kalansky, J.F., Cayan, D.R., Abatzoglou, J.T., 2020. Projected
1444 Changes in Reference Evapotranspiration in California and Nevada: Implications for
1445 Drought and Wildland Fire Danger. *Earth's Future* 8, e2020EF001736.
1446 <https://doi.org/10.1029/2020EF001736>

1447 Milly, P. C. D., & Dunne, K. A. (2017). A Hydrologic Drying Bias in Water-Resource Impact
1448 Analyses of Anthropogenic Climate Change. *JAWRA Journal of the American Water*
1449 *Resources Association*, 53(4), 822–838. <https://doi.org/10.1111/1752-1688.12538>

1450 Milly, P. C. D., Dunne, K. A., & Vecchia, A. V. (2005). Global pattern of trends in streamflow
1451 and water availability in a changing climate. *Nature*, 438(7066), 347–350.
1452 <https://doi.org/10.1038/nature04312>

1453 Mote, P. W., Hamlet, A. F., Clark, M. P., & Lettenmaier, D. P. (2005). Declining mountain
1454 snowpack in western north america*. *Bulletin of the American Meteorological Society*,
1455 86(1), 39–50. <https://doi.org/10.1175/BAMS-86-1-39>

1456 Musselman, K. N., Clark, M. P., Liu, C., Ikeda, K., & Rasmussen, R. (2017). Slower snowmelt in
1457 a warmer world. *Nature Climate Change*, 7(3), 214–219.
1458 <https://doi.org/10.1038/nclimate3225>

Deleted: ¶

Deleted: Welch, L.A., Allen, D.M., 2014. Hydraulic conductivity characteristics in mountains and implications for conceptualizing bedrock groundwater flow. *Hydrogeol J* 22, 1003–1026. <https://doi.org/10.1007/s10040-014-1121-5...>

1465 Musselman, K. N., Molotch, N. P., & Margulis, S. A. (2017). Snowmelt response to simulated
1466 warming across a large elevation gradient, southern Sierra Nevada, California. *The*
1467 *Cryosphere*, 11(6), 2847–2866. <https://doi.org/10.5194/tc-11-2847-2017>

1468 [National Operational Hydrologic Remote Sensing Center. \(2004\). Snow Data Assimilation](#)
1469 [System \(SNODAS\) Data Products at NSIDC. <https://doi.org/10.7265/N5TB14TC>](#)

Formatted: Border: Top: (No border), Bottom: (No border), Left: (No border), Right: (No border), Between : (No border)

1470 Neelin, J. D., Langenbrunner, B., Meyerson, J. E., Hall, A., & Berg, N. (2013). California Winter
1471 Precipitation Change under Global Warming in the Coupled Model Intercomparison
1472 Project Phase 5 Ensemble. *Journal of Climate*, 26(17), 6238–6256.
1473 <https://doi.org/10.1175/JCLI-D-12-00514.1>

Formatted: Font color: Text 1

1474 [Neitsch, S. L., Arnold, J. G., Kiniry, J. R., & Williams, J. R. \(2001\). Soil and Water Assessment](#)
1475 [tool \(SWAT\) user’s manual version 2000. Grassland Soil and Water Research Laboratory.](#)
1476 [Temple, TX: ARS.](#)

Formatted: Font color: Text 1

1477 Niraula, R., Meixner, T., Dominguez, F., Bhattarai, N., Rodell, M., Ajami, H., et al. (2017). How
1478 Might Recharge Change Under Projected Climate Change in the Western U.S.?
1479 *Geophysical Research Letters*, 44(20), 10,407-10,418.
1480 <https://doi.org/10.1002/2017GL075421>

1481 [Niu, G.-Y., et al. \(2011\). The community Noah land surface model with multiparameterization](#)
1482 [options \(Noah-MP\): 1. Model description and evaluation with local-scale measurements. *J.*](#)
1483 [Geophys. Res., 116, D12109, doi: 10.1029/2010JD015139.](#)

1484 [SMAP. \(2015\). Soil Moisture Active Passive. Retrieved October 18, 2018, from SMAP](#)
1485 [website: <https://smap.jpl.nasa.gov/>](#)

Formatted: Font color: Text 1

1486 [Siirila-Woodburn, E. R., Rhoades, A. M., Hatchett, B. J., Huning, L. S., Szinai, J., Tague, C., Nico,](#)
1487 [P. S., Feldman, D. R., Jones, A. D., Collins, W. D., and Kaatz, L.: A low-to-no snow future](#)

Formatted: Font: 12 pt, Font color: Black

1488 [and its impacts on water resources in the western United States, *Nature Reviews Earth and*](#)
1489 [Environment](#), <https://doi.org/10.1038/s43017-021-00219-y>, 2021.

1490 Pascolini-Campbell, M., Reager, J. T., Chandanpurkar, H. A., & Rodell, M. (2021). A 10 per cent
1491 increase in global land evapotranspiration from 2003 to 2019. *Nature*, 593(7860), 543–547.
1492 <https://doi.org/10.1038/s41586-021-03503-5>

1493 Payne, A. E., Demory, M.-E., Leung, L. R., Ramos, A. M., Shields, C. A., Rutz, J. J., et al. (2020).
1494 Responses and impacts of atmospheric rivers to climate change. *Nature Reviews Earth &*
1495 *Environment*, 1(3), 143–157. <https://doi.org/10.1038/s43017-020-0030-5>

1496 Persad, G. G., Swain, D. L., Kouba, C., & Ortiz-Partida, J. P. (2020). Inter-model agreement on
1497 projected shifts in California hydroclimate characteristics critical to water management.
1498 *Climatic Change*, 162(3), 1493–1513. <https://doi.org/10.1007/s10584-020-02882-4>

1499 Ralph, F. M., & Dettinger, M. D. (2011). Storms, floods, and the science of atmospheric rivers.
1500 *Eos, Transactions American Geophysical Union*, 92(32), 265–266.
1501 <https://doi.org/10.1029/2011EO320001>

1502 Ralph, F. Martin, Neiman, P. J., Wick, G. A., Gutman, S. I., Dettinger, M. D., Cayan, D. R., &
1503 White, A. B. (2006). Flooding on California’s Russian River: Role of atmospheric rivers.
1504 *Geophysical Research Letters*, 33(13). <https://doi.org/10.1029/2006GL026689>

1505 Rasmussen, R., Liu, C., Ikeda, K., Gochis, D., Yates, D., Chen, F., et al. (2011). High-Resolution
1506 Coupled Climate Runoff Simulations of Seasonal Snowfall over Colorado: A Process
1507 Study of Current and Warmer Climate. *Journal of Climate*, 24(12), 3015–3048.
1508 <https://doi.org/10.1175/2010JCLI3985.1>

Formatted: No underline

1509 Rhoades, A. M., Huang, X., Ullrich, P. A., & Zarzycki, C. M. (2016). Characterizing Sierra Nevada
1510 Snowpack Using Variable-Resolution CESM. *Journal of Applied Meteorology and*
1511 *Climatology*, 55(1), 173–196. <https://doi.org/10.1175/JAMC-D-15-0156.1>

1512 Rhoades, A. M., Ullrich, P. A., & Zarzycki, C. M. (2018a). Projecting 21st century snowpack
1513 trends in western USA mountains using variable-resolution CESM. *Climate Dynamics*,
1514 50(1), 261–288. <https://doi.org/10.1007/s00382-017-3606-0>

1515 Rhoades, A. M., Jones, A. D., & Ullrich, P. A. (2018b). The changing character of the California
1516 Sierra Nevada as a natural reservoir. *Geophysical Research Letters*, 45, 13,008– 13,019.
1517 <https://doi.org/10.1029/2018GL080308>

1518 Rhoades, A. M., Ullrich, P. A., Zarzycki, C. M., Johansen, H., Margulis, S. A., Morrison, H., et
1519 al. (2018c). Sensitivity of Mountain Hydroclimate Simulations in Variable-Resolution
1520 CESM to Microphysics and Horizontal Resolution. *Journal of Advances in Modeling Earth*
1521 *Systems*, 10(6), 1357–1380. <https://doi.org/10.1029/2018MS001326>

1522 Rhoades, A. M., Jones, A. D., O'Brien, T. A., O'Brien, J. P., Ullrich, P. A., & Zarzycki, C. M.
1523 (2020a). Influences of North Pacific Ocean domain extent on the western U.S. winter
1524 hydroclimatology in variable-resolution CESM. *Journal of Geophysical Research:*
1525 *Atmospheres*, 125, e2019JD031977. <https://doi.org/10.1029/2019JD031977>

1526 Rhoades, A. M., Jones, A. D., Srivastava, A., Huang, H., O'Brien, T. A., Patricola, C. M., et al.
1527 (2020b). The shifting scales of western U.S. landfalling atmospheric rivers under climate
1528 change. *Geophysical Research Letters*, 47, e2020GL089096.
1529 <https://doi.org/10.1029/2020GL089096>

1530 Rhoades, A. M., Risser, M. D., Stone, D. A., Wehner, M. F., & Jones, A. D. (2021). Implications
1531 of warming on western United States landfalling atmospheric rivers and their flood

1532 damages. *Weather and Climate Extremes*, 32, 100326,
1533 <https://doi.org/10.1016/j.wace.2021.100326>

1534 Richards, L. A. (1931). Capillary conduction of liquids through porous medium. *Journal of*
1535 *Applied Physics*, 1(5), 318–333. <https://doi.org/10.1063/1.1745010>

1536 Safeeq, M., Grant, G. E., Lewis, S. L., Kramer, M. G., & Staab, B. (2014). A hydrogeologic
1537 framework for characterizing summer streamflow sensitivity to climate warming in the
1538 Pacific Northwest, USA. *Hydrology and Earth System Sciences*, (18), 1–8.
1539 <https://doi.org/10.5194/hess-18-3693-2014>

1540 Safeeq, M., Grant, G.E., Lewis, S.L. and Tague, C.L. (2013), Coupling snowpack and groundwater
1541 dynamics to interpret historical streamflow trends in the western United States. *Hydrol.*
1542 *Process.*, 27: 655-668. <https://doi.org/10.1002/hyp.9628>

1543 Safeeq, Mohammad, Grant, G. E., Lewis, S. L., & Staab, B. (2015). Predicting landscape
1544 sensitivity to present and future floods in the Pacific Northwest, USA. *Hydrological*
1545 *Processes*, 29(26), 5337–5353. <https://doi.org/10.1002/hyp.10553>

1546 SCRIPPS Institution of Oceanography. (2017, April). Northern California Just Surpassed the
1547 Wettest Year on Record | Scripps Institution of Oceanography, UC San Diego. Retrieved
1548 from <https://scripps.ucsd.edu/news/northern-california-just-surpassed-wettest-year-record>

1549 Shukla, S., Safeeq, M., AghaKouchak, A., Guan, K., & Funk, C. (2015). Temperature impacts on
1550 the WY 2014 drought in California. *Geophysical Research Letters*, 4384–4393.
1551 [https://doi.org/10.1002/2015GL063666@10.1002/\(ISSN\)1944-8007.CALDROUGHT1](https://doi.org/10.1002/2015GL063666@10.1002/(ISSN)1944-8007.CALDROUGHT1)

1552 Son, K., & Tague, C. (2019). Hydrologic responses to climate warming for a snow-dominated
1553 watershed and a transient snow watershed in the California Sierra. *Ecohydrology*, 12(1),
1554 e2053. <https://doi.org/10.1002/eco.2053>

1555 Strachan, S., and Daly, C. (2017), Testing the daily PRISM air temperature model on semiarid
 1556 mountain slopes, *J. Geophys. Res. Atmos.*, 122, 5697– 5715, doi:10.1002/2016JD025920.

1557 Swain, D. L., Langenbrunner, B., Neelin, J. D., & Hall, A. (2018). Increasing precipitation
 1558 volatility in twenty-first-century California. *Nature Climate Change*, 8(5), 427–433.
 1559 <https://doi.org/10.1038/s41558-018-0140-y>

1560 Tague, C., & Peng, H. (2013). The sensitivity of forest water use to the timing of precipitation and
 1561 snowmelt recharge in the California Sierra: Implications for a warming climate. *Journal of*
 1562 *Geophysical Research: Biogeosciences*, 118(2), 875–887.
 1563 <https://doi.org/10.1002/jgrg.20073>

1564 Tang, G., Li, S., Yang, M., Xu, Z., Liu, Y., & Gu, H. (2019). Streamflow response to snow regime
 1565 shift associated with climate variability in four mountain watersheds in the US Great Basin.
 1566 *Journal of Hydrology*, 573, 255–266. <https://doi.org/10.1016/j.jhydrol.2019.03.021>

1567 The NCAR Command Language (Version 6.6.2) (2021). Boulder, Colorado:
 1568 UCAR/NCAR/CISL/TDD, 851 <http://dx.doi.org/10.5065/D6WD3XH5>.

1569 [Trefry, M.G.; Muffels, C. \(2007\). "FEFLOW: a finite-element ground water flow and transport](#)
 1570 [modeling tool". *Ground Water*. 45 \(5\): 525–528. doi:10.1111/j.1745-6584.2007.00358.x](#)

1571 Vicuna, S., & Dracup, J. A. (2007). The evolution of climate change impact studies on hydrology
 1572 and water resources in California. *Climatic Change*, 82(3), 327–350.
 1573 <https://doi.org/10.1007/s10584-006-9207-2>

1574 Vicuna, Sebastian, Maurer, E. P., Joyce, B., Dracup, J. A., & Purkey, D. (2007). The Sensitivity
 1575 of California Water Resources to Climate Change Scenarios1. *JAWRA Journal of the*
 1576 *American Water Resources Association*, 43(2), 482–498. [https://doi.org/10.1111/j.1752-](https://doi.org/10.1111/j.1752-1688.2007.00038.x)
 1577 [1688.2007.00038.x](https://doi.org/10.1111/j.1752-1688.2007.00038.x)

Formatted: Font color: Text 1

1578 Wang, S.-Y. S., Yoon, J.-H., Becker, E., & Gillies, R. (2017). California from drought to deluge.

1579 Nature Climate Change, 7(7), 465. <https://doi.org/10.1038/nclimate3330>

Deleted: <https://doi.org/10.1038/nclimate3330>

1580 [Welch, L.A., Allen, D.M., 2014. Hydraulic conductivity characteristics in mountains and](#)

1581 [implications for conceptualizing bedrock groundwater flow. Hydrogeol J 22, 1003–1026.](#)

1582 <https://doi.org/10.1007/s10040-014-1121-5>

Formatted: Font color: Auto

1583 Wu, C., Liu, X., Lin, Z., Rhoades, A. M., Ullrich, P. A., Zarzycki, C. M., et al. (2017). Exploring

1584 a Variable-Resolution Approach for Simulating Regional Climate in the Rocky Mountain

1585 Region Using the VR-CESM. *Journal of Geophysical Research: Atmospheres*, 122(20),

1586 10,939-10,965. <https://doi.org/10.1002/2017JD027008>

1587 Zarzycki, C. M., Levy, M. N., Jablonowski, C., Overfelt, J. R., Taylor, M. A., and Ullrich, P. A.

1588 (2014). Aquaplanet Experiments Using CAM's Variable-Resolution Dynamical Core.

1589 *Journal of Climate* 27, 14, 5481-5503, <https://doi.org/10.1175/JCLI-D-14-00004.1>

1590

1591

1592

1593

